

Full capacitance-matrix effects in driven Josephson-junction arrays

Frank Gibbons¹, A. Góngora-T², and Jorge V. José^{1,2}

¹*Physics Department and Center for Interdisciplinary Research on Complex Systems,
Northeastern University, Boston, MA 02115, USA**

²*Instituto de Física, Universidad Nacional Autónoma de México,
Apdo. Postal 20-364, 01000 México D. F., México*

(February 1, 2008)

We study the dynamic response to external currents of periodic arrays of Josephson junctions, in a resistively capacitively shunted junction (RCSJ) model, including *full capacitance-matrix effects*. We define and study three different models of the capacitance matrix $C_{\vec{r},\vec{r}'}$: *Model A* includes only mutual capacitances; *Model B* includes mutual and self capacitances, leading to exponential screening of the electrostatic fields; *Model C* includes a dense matrix $C_{\vec{r},\vec{r}'}$ that is constructed approximately from superposition of an exact analytic solution for the capacitance between two disks of finite radius and thickness. In the latter case the electrostatic fields decay algebraically. For comparison, we have also evaluated the full capacitance matrix using the MIT FASTCAP algorithm, good for small lattices, as well as a corresponding continuum effective-medium analytic evaluation of a finite-voltage disk inside a zero-potential plane. In all cases the effective $C_{\vec{r},\vec{r}'}$ decays algebraically with distance, with different powers. We have then calculated current–voltage characteristics for DC+AC currents for all models. We find that there are novel giant capacitive fractional steps in the I-V's for *Models B* and *C*, strongly dependent on the amount of screening involved. We find that these fractional steps are quantized in units inversely proportional to the lattice sizes and depend on the properties of $C_{\vec{r},\vec{r}'}$. We also show that the capacitive steps are not related to vortex oscillations but to localized screened phase-locking of a few rows in the lattice. The possible experimental relevance of these results is also discussed.

I. INTRODUCTION

There has been considerable recent interest in the study of the dynamic response of two-dimensional Josephson-junction arrays (JJA) under different physical conditions. This interest has both theoretical and experimental motivations¹. Experimentally, recent advances in photolithographic micro-fabrication techniques have allowed the manufacture of these arrays with specific tailor-made properties¹. The arrays can be made with proximity-effect, i.e., superconducting–metal–superconducting (SNS) junctions, or with superconducting–insulating–superconducting (SIS) junctions. In the SNS case there is essentially zero capacitance between the superconducting islands. In the SIS case the electrodes that form the junctions have nonzero

self and mutual capacitances that can, as discussed in this paper, significantly influence the physical properties of the arrays. Theoretically, the arrays are described in terms of a large set of coupled, non-linear differential equations, overdamped in the SNS case and underdamped in the SIS case. The SNS arrays have been studied more extensively, for they can be fabricated with more ease, better uniformity and larger lattice sizes. In the SNS arrays the critical currents can be large and thus self-induced magnetic fields must be taken into account, through the inclusion of Faraday's induction law to fully describe the experimental systems^{2–4}. In contrast, in SIS arrays the critical currents are relatively low and self-induced fields are usually not significant. In this paper we consider the SIS case where the electrostatic properties of the junctions in the array are of importance, while the inductances are not included here.

When the arrays are driven by DC+AC currents, non-equilibrium stationary coherent oscillatory vortex states may appear, both in the SNS and SIS arrays. Experimentally, giant Shapiro steps (GSS) have been observed in the I-V characteristics of SNS arrays in zero⁵ and rational magnetic field frustrations⁶. The frustration is defined by $f = \Phi/\Phi_0$, where Φ is the average applied magnetic flux per plaquette, and $\Phi_0 = h/2e$ is the magnetic flux quantum. Coherent oscillations of ground-state field-induced vortices are responsible for the existence of the *fractional* GSS when $f = p/q$, with p and q relative primes⁶. This interpretation was successfully verified in numerical simulations when the junctions in the array were modeled by the resistively shunted junction (RSJ) model^{7,8}. Half-integer steps have also been found in zero-field topologically disordered SNS arrays, due to a special oscillatory vortex pattern termed the *axisymmetric coherent vortex state*, or ACVS⁹. Fundamentally different half-integer Shapiro steps have also been seen in capacitive array models, with $f = 0$, when the capacitance matrix includes only the mutual capacitance between superconducting islands¹⁰. In all the cases discussed above the steps found in the I-V characteristics were microscopically due to the collective coherent oscillatory motion of dynamically or magnetically induced vortices.

Experimental papers on SIS arrays do report on the importance of electric field screening, or capacitive effects, in particular when the junctions are of submicron size¹¹, but also when they are large¹². In the cases when the electrostatic screening length is smaller than the array

size, the screening may affect the array's transport properties in a significant way. Most work that has included capacitive effects, however, has done so considering only nearest-neighbor mutual capacitances. To be more specific, consider an array formed by N conducting islands where the capacitance of the whole array can be characterized by a matrix $C_{\vec{r},\vec{r}'}$, where \vec{r} and \vec{r}' are vectors denoting the locations of two electrostatically interacting islands. The dynamical equations of motion for a driven array that includes general capacitive affects can be written as an extension of the resistively capacitively shunted junction (RCSJ) model. This model, which includes mutual capacitances, has been successful in explaining the giant Shapiro steps described above. The corresponding equations read:

$$\begin{aligned} \beta_c \sum_{\vec{r}'} C_{\vec{r},\vec{r}'} \ddot{\theta}_{\vec{r}'} + \sum_{\vec{r}'} G_{\vec{r},\vec{r}'}^{-1} \dot{\theta}_{\vec{r}'} + \sum_{\hat{\mu}} \sin(\theta_{\vec{r}+\hat{\mu}} - \theta_{\vec{r}}) \\ = i_{\text{ext}}(\vec{r}, t) \equiv i_{dc} + i_{ac} \sin(2\pi\nu t). \end{aligned} \quad (1)$$

Here $\theta_{\vec{r}}$ is the phase of the Ginsburg–Landau order parameter for the \vec{r} -th island; G^{-1} is the inverse lattice Green function in two dimensions (2D) (i.e., the discrete Laplacian); the $\sum_{\hat{\mu}}$ indicates a sum over nearest neighbors. $i_{\text{ext}}(\vec{r}, t)$ is the external current injected at each lattice site \vec{r} , with both a DC and an AC component that oscillates at frequency ν . The currents are expressed in units of the junction critical current I_c ; time is measured in units of the characteristic time $1/\omega_c = \hbar/(2eRI_c)$, with R the normal-state junction resistance, e the electronic charge, and $\hbar = h/2\pi$, with h Planck's constant. The capacitance matrix entries are normalized by the single-junction dissipation, or Stewart–McCumber, parameter $\beta_c = 2eR^2I_cC_m/\hbar$, where C_m is the mutual capacitance of a single junction.

The purpose of this paper is to study solutions to Eq. (1) for different ever-more-realistic approximations to the $C_{\vec{r},\vec{r}'}$ matrix. Just as was done in the inductive case^{2,3,13}, here we consider the array response to external currents when $C_{\vec{r},\vec{r}'}$ goes from being short- to long-ranged. We concentrate mostly on the régime that does not show chaotic solutions in the single-junction case, for extra complications may arise in that case that can complicate the analysis further. We also only consider the semiclassical regime, where the Josephson energy dominates the charging energy. As in previous studies we do find giant steps in the I-V characteristics in the models considered here. In contrast, however, to the GSS described above, the ones described in this paper are not associated with collective vortex oscillations. Instead, depending on the specific model for the capacitance matrix, they are related to the phase-locking of specific row of junctions to the external drive.

Here we introduce and study different approximate models for the capacitance matrix. We know that we cannot exactly calculate the general $C_{\vec{r},\vec{r}'}$ matrix by simply giving the geometric configurations of the conductors. We start then by assuming that the $C_{\vec{r},\vec{r}'}$ has only

the nearest-neighbor mutual component, which reduces $C_{\vec{r},\vec{r}'}$ to a tridiagonal form. This is the model that has been studied most in the past (see Ref. 10). Including the self-capacitances, which can be done experimentally by putting a ground plane underneath the array, leads to screening in $C_{\vec{r},\vec{r}'}$. The self- plus mutual-capacitance matrix approximation reduces the complexity of the full $C_{\vec{r},\vec{r}'}$ significantly. Making this approximation physically means that the electric field lines between charges will be confined to the plane of the array, with logarithmic interaction with distance. Here we want to go beyond these approximations and take into account the fact that the field lines are experimentally three-dimensional in nature, so we need to consider further elements in $C_{\vec{r},\vec{r}'}$. We must then resort to approximate representations of this matrix. We have followed several different ways to estimate the behavior of $C_{\vec{r},\vec{r}'}$, some analytic, some numeric. On the analytic side, we evaluated the capacitance of two disks of finite thickness and radius in a plane^{14,15}. We use the result obtained from this calculation to fill in, using approximate superposition, what would be the matrix elements of a full $C_{\vec{r},\vec{r}'}$ matrix. This approach is similar to the one followed in the full inductance calculations that gave rather good results¹³. To ascertain the nature of this approximation, next we used the MIT FASTCAP algorithm¹⁶ that numerically evaluates the $C_{\vec{r},\vec{r}'}$ for small systems. To further understand the FASTCAP results we also evaluated the capacitance of a finite potential disk of finite radius embedded in an infinite grounded plane. We looked at this problem since it represents a type of effective-medium approximation of the FASTCAP algorithm. In all these estimates of the $C_{\vec{r},\vec{r}'}$ matrix we found that it decays algebraically with distance. The rate of decay, i.e., the power of the decay is different in the various model approximations. This leads to some quantitative difference in the corresponding I-V results, but we expect that qualitatively they are correct, and certainly when compared with the exponentially decaying behavior of the self–mutual approximation to $C_{\vec{r},\vec{r}'}$.

In studying the behavior of the I-V's of the full-capacitance model, we have found other types of giant capacitive voltage steps in the I-V curves, which are of a very different origin from the ones studied previously. In this paper, we define a *row* as a series of neighboring junctions along the direction transverse to the current. Under certain conditions, we have observed these *giant capacitive fractional steps* (GCFS), which are caused by *phase-locking* of junctions in a given row to the external drive, with no significant phase-locking between rows. The array exhibits the phase-locking behavior which underlies the GCFS, but we find that this does not occur throughout the entire array. Rather, it only occurs in certain rows near the edge of the array, due to screening. We discuss these results in more detail in the main body of the paper.

The outline of the paper is the following: In Section II we present the equations that describe the different models mentioned above, as well as briefly discussing the

methods we used to study them. We also present some analytical results which we used in our analysis and to fill out the entries of the full capacitance matrix. Section III discusses the bulk of our results and their analysis, for the cases where the driving current is purely DC or a combination DC+AC. We study the I-V's, spectral functions, and topological phase and current distributions, to support our view that the steps are indeed generated by phase-locking of a few rows of junctions (rather than the entire array), and not by the presence of a stable vortex configuration, as is the case with other giant fractional steps. Finally, in Section IV we summarize and discuss our results.

II. CAPACITANCE-MATRIX MODELS

In this section we proceed to define the different capacitance matrix models studied and compared in this paper. Our goal is to solve Eq. (1) for different $C_{\vec{r},\vec{r}'}$ matrix models. We begin by converting the set of $N \equiv L_x \times L_y$ second-order ordinary differential equations into $2N$ first-order equations. Explicitly, we define the variables $z_{\vec{r}}$ and $\dot{z}_{\vec{r}}$ that satisfy the equations,

$$z_{\vec{r}} = \dot{\theta}_{\vec{r}}, \quad (2)$$

$$\dot{z}_{\vec{r}} = \frac{1}{\beta_c} \sum_{\vec{r}'} C_{\vec{r},\vec{r}'}^{-1} \left(i_{\text{ext}}(\vec{r}') - \sum_{\vec{r}''} G_{\vec{r}',\vec{r}''}^{-1} z_{\vec{r}''} - \sum_{\hat{\mu}} \sin(\theta_{\vec{r}'+\hat{\mu}} - \theta_{\vec{r}'}) \right), \quad (3)$$

where the indices \vec{r}, \vec{r}' , and \vec{r}'' run from 1 to N , that is, over the whole array. Periodic boundary conditions are used in the direction perpendicular to the current. A schematic of the arrays under study is shown in Fig. 1. In order to simulate large arrays, it is useful to use the general properties of the capacitance matrix that arise from the positivity of the total electrostatic energy of the array of electrodes. Specifically, $C_{\vec{r},\vec{r}'} > 0, \forall \vec{r} = \vec{r}', C_{\vec{r},\vec{r}'} < 0, \forall \vec{r} \neq \vec{r}'$, and $C_{\vec{r},\vec{r}} \geq \sum_{\vec{r}' \neq \vec{r}} |C_{\vec{r},\vec{r}'}|$. In addition to these properties, we have translational invariance in a periodic array, so that we can write $C(\vec{r}, \vec{r}') \equiv C(|\vec{r} - \vec{r}'|)$, which allows for a significant simplification in the calculation of $C_{\vec{r},\vec{r}'}$. Our approach parallels the scheme used in the dynamic study of inductive Josephson-junction arrays², and we consider here the following three distinct capacitive models:

Model A: In this case we consider only the contributions by the mutual capacitances between electrodes in the array. Here the capacitance matrix is simply tridiagonal, i.e.,

$$C_{\vec{r},\vec{r}'} = 4\delta_{\vec{r},\vec{r}'} - \delta_{\vec{r},\vec{r}'} \pm \hat{e}_x - \delta_{\vec{r},\vec{r}'} \pm \hat{e}_y \equiv G_{\vec{r},\vec{r}'}^{-1}$$

with \hat{e}_x and \hat{e}_y are unitary vectors along the x - and y -directions. This model has been studied by many

authors^{1,10,13}, both for ordered and disordered arrays, and some results are already known.

Model B: This model extends *Model A* by including the self-capacitance term in the capacitance matrix as:

$$C_{\vec{r},\vec{r}'} = (4 + r_c) \delta_{\vec{r},\vec{r}'} - \delta_{\vec{r},\vec{r}'} \pm \hat{e}_x - \delta_{\vec{r},\vec{r}'} \pm \hat{e}_y,$$

where $r_c = |C_s/C_m|$, and C_s and C_m are the self-capacitance and the mutual capacitances, respectively. This model tends to *Model A* in the limit $r_c \rightarrow 0$. In the continuum limit the inverse of the capacitance matrix becomes

$$C^{-1}(r) \simeq \frac{1}{2\pi C_m} K_0(\sqrt{r_c} r),$$

with $K_0(z)$ is the modified Bessel function of zeroth order. Asymptotically, we have that $K_0(z) \sim -\ell n z$, for $z \ll 1$, and $K_0(z) \sim \sqrt{\frac{\pi}{2z}} e^{-z}$, for $z \gg 1$. We see that when the self-capacitance is very small the interactions are essentially logarithmic with distance, and for large C_s they are exponential. We define then the screening length as $\Lambda_0 = \frac{1}{\sqrt{r_c}}$. We will describe our results for the models studied here as functions of the parameters, β_c , ν and Λ_0 , or r_c .

Model C: Here we consider the capacitive effects of all conductors on each other. This means that the capacitance matrix is dense, and the specific form of the individual entries depends on the details of how we model the conductors in the array. We have used several routes to analyze the long-range interaction that gives approximate full capacitance-matrix models. Most of our I-V calculations are based on a $C_{\vec{r},\vec{r}'}$ obtained by an approximate superposition model from an exact analytic solution for the capacitance of two circular disks of finite thickness and radius^{14,15}. We review the derivation of this result in detail in the Appendix.

We place each disk at a lattice site in a square array. For the total capacitance matrix we use simple superposition of the capacitances between any two disks, as done in the inductive case, so as to get

$$C_{\vec{r},\vec{r}'} = C(i, j) = \frac{1}{4 \tanh^{-1} \left(\sqrt{1 - \frac{D^2}{i^2 + j^2}} \right)}, \quad (4)$$

and

$$C_m \equiv C(i = 1, j = 0) = \frac{1}{4 \tanh^{-1} \left(\sqrt{1 - D^2} \right)}, \quad (5)$$

where $\vec{r} - \vec{r}' = i\hat{e}_x + j\hat{e}_y$, i and j are integers, D is the diameter of a disk and R is the distance between their centers (see Fig. 2). Note that the magnitude of D defines the packing of the disks as shown in the figure. The two-disk expression for $C(i, j)$ given above allows us to go from weak to strong screening by just varying D . For different values of D , $C(i, j)$ has an initial rapid decay with distance and then it decays algebraically. We show

in Fig. 3 the behavior of the effective full $C(i, j)$ matrix for some values of D .

For comparison to the two-disk model result, we also have used the FASTCAP numerical capacitance extraction tool developed at MIT¹⁶. This algorithm quantitatively calculates the capacitance matrix for a given distribution of conductors. Whan et al. [19] have studied one and two-dimensional arrays of circular dots using FASTCAP. They also obtained a power-law decay with exponent close to one. We also use their result in the evaluation of DC IV's in Section III. We have also explicitly used FASTCAP, to compute $C_{\vec{r}, \vec{r}'}$ for an 8×8 array of square plates of various thicknesses, ranging from 1000 Å to 35000 Å. We took the dimensions used by van der Zant *et al.*¹⁷. A log-log plot of the capacitance versus the distance is shown in Fig. 3. This capacitance result tends to the two-disk array model for a specific value of D , but differs for others. The essence of the result, however, is that the off-diagonal capacitance matrix decays algebraically.

The FASTCAP approach is limited in that the arrays that can be simulated are relatively small. (For example, 11×11 was the largest size possible on a fast DEC Alpha with 196 MB RAM.) In the FASTCAP algorithm the capacitance matrix entries are calculated iteratively, by successively grounding all but one of the conductors, and holding it at a fixed nonzero potential. The limitations of this approach are that it is time-consuming and not many parameter values can be easily considered. In contrast, the two-disk model is more flexible and allows the study of larger lattices and a wider range of parameter values.

In order to further understand how the capacitance matrix behaves we have also analytically calculated the electrostatic potential, and then the capacitance, of a circular disk of finite width set at a fixed potential embedded in a conducting plane set at zero potential. The disk is of radius $s = D/2$ located at the coordinate origin and at a finite nonzero potential V_0 , while the conducting plane is at zero potential. We considered this problem since it is, in a sense, similar to the lattice algorithm used in FASTCAP and it also gives us another evaluation of the capacitance in the continuum limit. We want to calculate the potential outside of the plane and thus start from the general expression for the potential at point \vec{r} given by (see Jackson¹⁴)

$$V(\vec{r}) = -\frac{1}{4\pi} \oint_S V(\vec{r}') \frac{\partial F(\vec{r}, \vec{r}')}{\partial z'} \Big|_{\vec{n}=\vec{0}} dA'.$$

Here $F(\vec{r}, \vec{r}')$ is the Green function for two unit charges at z and z' , \vec{n} is the normal vector to the surface of integration S , and dA' the surface differential. In cylindrical coordinates (ρ, φ, z) , $F(\vec{r}, \vec{r}')$ is given by

$$F(\rho, \rho', \phi, \phi', z, z') = \frac{1}{\sqrt{\rho^2 + \rho'^2 - 2\rho\rho' \cos\gamma + (z - z')^2}} - \frac{1}{\sqrt{\rho^2 + \rho'^2 - 2\rho\rho' \cos\gamma + (z + z')^2}},$$

where $\gamma = (\varphi - \varphi')$. After evaluation of the z -derivative of F we get

$$V(\rho, \varphi, z) = \frac{1}{2\pi} \int_0^s \int_0^{2\pi} \frac{z V_0 \rho' d\rho' d\varphi'}{(\rho^2 + \rho'^2 - 2\rho\rho' \cos\gamma + z^2)^{3/2}}.$$

The surface charge is given by the expression

$$\sigma = -\frac{1}{4\pi} \frac{\partial V(\rho, \varphi, z)}{\partial z} \Big|_{z=0},$$

which gives the integral,

$$\sigma = -\frac{V_0}{8\pi^2} \int_0^s \int_0^{2\pi} \frac{\rho' d\rho' d\varphi'}{[\rho^2 + \rho'^2 - 2\rho\rho' \cos(\varphi - \varphi')]^{3/2}}.$$

The ρ' -integral can be evaluated explicitly giving

$$\sigma = -\frac{V_0}{8\pi^2} \left(\frac{1}{\rho} \int_0^{2\pi} \frac{d\varphi'}{\sin^2(\varphi - \varphi')} - \int_0^{2\pi} \frac{d\varphi'}{\sin^2(\varphi - \varphi') \sqrt{\rho^2 + s^2 - 2\rho s \cos(\varphi - \varphi')}} + \frac{s}{\rho} \int_0^{2\pi} \frac{\cos(\varphi - \varphi') d\varphi'}{\sin^2(\varphi - \varphi') \sqrt{\rho^2 + s^2 - 2\rho s \cos(\varphi - \varphi')}} \right).$$

The first integral is zero while the last two integrals are elliptic in nature and are given in tables. Here we are interested in the long-distance behavior and thus expand the integrals in the index of the elliptic integrals. We can then obtain the corresponding capacitance, defined as charge divided by voltage and the volume of the disk of thickness h , as

$$C_D = -\frac{1}{8\pi^2 h} \left(\frac{1}{\rho^2 s - s^3} + \frac{4\rho^3}{(\rho - s)^4 (\rho^2 - s^2)} + \frac{6\rho^4 s^2 (4\rho^2 - 2s^2 - 2s\rho)}{(\rho - s)^9 (\rho^2 - s^2)} + \frac{8\rho^6 s^4 (6\rho^2 - 4s^2 - 2s\rho)}{(\rho - s)^{13} (\rho^2 - s^2)} + \dots \right). \quad (6)$$

One of the advantages of this result is that it shows that there are different algebraic contributions depending on the ρ -range. We show in Fig. 3 that for small ρ this expression is almost linear in the log-log plot but not exactly so for larger distances.

All the results for the full capacitance analyses are shown in Fig. 3. There we see that the rates of decay are different depending on the approximation but the basic nature of the result is the algebraic or nonexponential decay of the off-diagonal elements of the capacitance matrix. Note, however, that the comparisons between capacitive models here are qualitative since the definition of the parameters in the different models is not exactly the same. We conclude that the two-disk model contains the essence of a full capacitance matrix and thus have done most of our calculations using this model.

A. Calculational approach

In solving the dynamical equations of motion a good amount of time is spent in calculating the inverse of the capacitance matrix. Inversion of $C_{\vec{r},\vec{r}'}$ may be tackled in different ways, depending on how much we know about it.

In the case when $C_{\vec{r},\vec{r}'}$ is tri-diagonal, it has only mutual or mutual+self capacitances and its Fourier representation in momentum space is also tri-diagonal. Taking advantage of this form, we can use an optimized (lower-upper) LU decomposition algorithm¹⁶ to invert $C_{\vec{r},\vec{r}'}$, such that the calculation time grows like $\sim N \log N$, rather than $\sim N^2$. In the case when $C_{\vec{r},\vec{r}'}$ is dense, we can still use the translational invariance to go to momentum space, although the multiplication (again by LU decomposition) will now grow like $\sim N^2$.

Another possibility is when we already know the inverse of $C_{\vec{r},\vec{r}'}$ and we just need an efficient way to carry out the multiplications. Once again, translational invariance can be used to reduce the complexity of this task. We can rewrite equation Eq. (3) using the definition $s(\vec{r}) \equiv i_{\text{ext}}(\vec{r}) - \sum_{\vec{r}'} G_{\vec{r},\vec{r}'}^{-1} z_{\vec{r}'} - \sum_{\hat{\mu}} \sin(\theta_{\vec{r}+\hat{\mu}} - \theta_{\vec{r}})$, as

$$\dot{z}_{\vec{r}} = \frac{1}{\beta_c} \sum_{\vec{r}'} C^{-1}(\vec{r}, \vec{r}') s(\vec{r}'). \quad (7)$$

As pointed out by Phillips *et al.*³, this has the form of a convolution, and can thus be evaluated in $\sim N^2$ multiplications, plus the cost of performing the Fourier transform ($\sim N \log N$), as opposed to $\sim N^4$ for the direct multiplication. Because we do not have periodicity in the current direction, in order to obtain a linear convolution¹⁸ we use the standard ‘zero-padding’ techniques as is done in digital signal processing. The integration in time is carried out mostly by the second-order Runge–Kutta (RK) algorithm.

B. Physical quantities calculated

One of the quantities we are interested in computing is the total voltage drop per junction in the array given by the Josephson relation,

$$\langle V(t) \rangle \equiv \frac{2e}{h\nu} \frac{1}{L_x(L_y - 1)} \sum_{i=1}^{L_x} \left(\dot{\theta}_{i,L_y-1} - \dot{\theta}_{i,1} \right). \quad (8)$$

The Josephson-junction arrays studied before exhibited steps of two very different origins: the integer steps, due to coherent phase-slippage, and the fractional steps, due to vortex motion. It is then important to see whether or not there are vortices associated with possible quantized fractional steps in the I-V’s. We define two types of dual lattice vorticities: one topological and one current related. The topological vorticity is defined as

$$n(\vec{R}) = \frac{1}{2\pi} \text{nint} \left(\sum_{P\{\vec{R}\}} \Delta\theta \right), \quad (9)$$

and the current vorticity by

$$c(\vec{R}) = \sum_{P\{\vec{R}\}} \sin(\Delta\theta). \quad (10)$$

Here $P\{\vec{R}\}$ denotes the sum around the four bonds enclosing the plaquette at position \vec{R} , and $\text{nint}(x)$ is the nearest integer to x . It is important to remember that the phase difference $\Delta\theta$ is restricted to the range $[-\pi, \pi)$. The fractional steps which we have found in the capacitive models are not vortex related but it was important to calculate the vorticities to check that. We do not show figures since there is nothing to see.

In particular in *Model C* we find that there are neither topological vortices nor eddy current vortex produced in the fractional steps. This appears to be true even when we let the system evolve for 500 periods of the driving current, long after the voltage has stabilized. In addition, in the FASTCAP model, when we look at the eddy vortices, we find that, apart from a short-lived transient, no vortices are present.

To further understand what is happening we also have looked at the spectral function defined as

$$S(\nu) = \lim_{\tau \rightarrow \infty} \left| \frac{1}{\tau} \int_0^\tau V(t) e^{i2\pi\nu t} dt \right|^2. \quad (11)$$

For integer steps $S(\nu)$ has peaks at frequencies $n\nu$, for periodic and disordered arrays⁷. This is consistent with the resonant nature of the integer steps. For the disordered arrays that produce the ACVS state there are half-integer vortex steps, corresponding to an $S(\nu)$ that has additional peaks at frequencies $n\nu/2$.

III. RESULTS

In this Section we consider the response of *Models A–C* under different current-driven conditions. First we consider the case when the array is subjected to a DC external current and next when there is a DC+AC current drive. We also look at other physical measures defined above, that further help us in the analysis of the results.

A. DC current–voltage characteristics

Josephson-junction arrays driven only by a DC current have been studied before in the overdamped case and also in *Model A*¹. Here we examine the I-V’s for 8×8 arrays in *Model C* based on the two-disk approximation as well as a square plate model based on a FASTCAP calculation.

We have computed the DC I-V's for *Model C* in a DC drive for different values of the parameter, D . When $D \lesssim 1$, and with $\Lambda_0 \gg L_x, L_y$, there is basically no screening and thus the I-V's have the usual quadratic form¹³:

$$V = \sqrt{i_{dc}^2 - 1}. \quad (12)$$

In Fig. 4 we show the behavior of the I-V's for two extreme values of the disk diameter D . As D slowly decreases from 1.0, we find little change in the shape of the I-V's until $D \sim 0.7$. At this point, the I-V rather loses its smooth curved shape, and assumes a piecewise linear form characterized by a very sudden increase, and then to linear ohmic behavior as the current is increased. We also note a slightly lower critical current for the latter case.

Next we also calculated the I-V in the FASTCAP disk model considered in Ref. 19 in a régime close to that of *Model C* considered above. In this case the results shown in Fig. 5 are somewhat more tentative, for we may be operating outside the régime in which the FASTCAP model is valid. Qualitatively, the I-V's display the transition from a smooth shape for a large value of \tilde{D} (defined as a normalized diameter of the disk) to piecewise linear at smaller \tilde{D} -values. Note that quantitatively this length \tilde{D} is not exactly the same as the one defined for *Model C*. The conclusion from these calculations is, however, that the results evaluated with both models are qualitatively, if not quantitatively similar.

B. DC+AC current–voltage characteristics

Here we present results for DC+AC driven capacitive JJA and compare results for *Models A*, *B*, and *C*. *Model A* has been studied to some extent and we briefly mention those results here, but we will be mostly concerned with results for *Models B* and *C*.

1. Model A: Mutual capacitances only.

This case has been studied in Ref. 10 mostly in the transition region between regular and chaotic behavior for the single-junction problem. Apart from the integer giant Shapiro steps Hagenaars *et al.*¹⁰ find the formation of a half-integer step, within a range of values of β_c which include chaos in the single junction, with characteristics similar to those of the ACVS state mentioned in the introduction. In our analysis we mostly stay away from the single-junction chaotic state, and do not see the half-integer steps. Next we look at what happens when there is screening in the capacitive models.

2. Model B: Self+mutual capacitances only

Here we present results when the capacitance matrix is composed of the self capacitance of each island to ground plus the mutual capacitance of each island to *only* its nearest neighbors. The time-step used in the second-order Runge–Kutta calculations was 0.05 for all the results in this section, with a current grid of $\delta i_{dc}/i_c = 0.005$. Except where otherwise noted, averaging was carried out over 6×10^4 time-steps, after throwing out the first 2×10^4 for equilibration.

As mentioned before, addition of the self capacitance to *Model A* introduces exponential screening that for large distances is measured by the screening length $\Lambda_0 = \sqrt{C_m/C_s} = 1/\sqrt{r_c}$. Our results were obtained principally on an 8×8 array, but we have seen similar behavior in much larger arrays (e.g., 40×40 , see Fig. 6). We find that there are new giant capacitive fractional steps (GCFS) as we vary Λ_0 . When such steps occur, they appear as multiples of $\frac{n}{L_y-1}$, where $n = 1, 2, 3$ and possibly 4.

The results obtained when $\Lambda_0 \gg L_y$ were, as must be, identical to those obtained with the capacitance matrix composed of *Model A*. The existence of these integer-steps depends on the locked-in coherent phase oscillation of all junctions in the array with the drive. On reducing the screening length to a value smaller than the array size, the integer-steps began to disappear, and then new steps appeared at fractional values of the normalized voltage.

It can be seen in Fig. 7 that, for $\Lambda_0 > L_y$, the width of the integer-step is entirely unaffected by screening. As Λ_0 approaches $L_y/2$, the step at $n = 1$ begins to shrink, and as $\Lambda_0 \rightarrow 1$, the step is rapidly destroyed. In Fig. 8 we show the change in the width of the $n = 1$ step as a function of Λ_0 .

We then examined the step width for the GCFS $\frac{2}{7}$ -step as functions of the frequency ν , β_c and Λ_0 . As can be seen from Fig. 9, the appearance of this step is quite strongly dependent on the drive frequency, and it is absent for frequencies 15% greater than or less than $\nu = 0.1$, with $\beta_c = 0.50$. Next we fixed ν , and looked at the width of the fractional steps, as a function of β_c . Our results are shown in Fig. 10. The $\frac{1}{7}$ - and $\frac{2}{7}$ -steps are seen to appear for $\beta_c \sim 0.3$, reach their maximum values at around $\beta_c \sim 0.7$, and then slowly disappear, as β_c is increased. All fractional and integer steps have disappeared by the time β_c has reached the value 3.0. Each step has a *maximal screening length* denoted Λ_0^{\max} for which its width is maximized, and the lower the order of the step, the smaller its Λ_0^{\max} . We mostly stayed outside the range of β_c for which the single-junction behavior is chaotic, though Fig. 10 shows that chaos is not necessary to generate the GCFS.

We then fixed both $\nu = 0.1$ and $\beta_c = 0.6$ (parameters for which the step-widths appear to be maximized), and looked at how the step-width varies as a function of

Λ_0 . The results are shown in Fig. 11. We decreased the screening length from a large value until Λ_0 had reached half the array size, i.e., $\Lambda_0 \sim 4$. At this point, the fractional step size jumps up rather rapidly to almost its maximum value, remains there until the screening length has reached the value 1.0, and then falls rapidly to zero once again. This behavior can be seen to happen for both the $\frac{1}{7}$ - and $\frac{2}{7}$ -steps.

We obtained these steps by starting up from a lower value of i_{dc} , since one cannot see the step by simply setting the value of i_{dc} according to the expected step values in the I-V's. The fractional steps are hysteretic, as indicated by the inset in Fig. 11. This is a typical property of *Model A* arrays, and has been seen in previous studies, whose authors interpret them as evidence of vortex inertia¹³. Both of these facts indicate that the GCFS are metastable, since their existence depends on the previous history conditions of the array.

Usually, the appearance of a step at a voltage $V = \frac{p}{q}$ indicates that a process with frequency $\frac{p}{q}\nu$ underlies the production of the step. This should be visible in the Fourier power spectrum of the array voltage. For the integer steps that is what we see but not so for the GCFS, which signals that they are of a different nature to the steps studied before, as we further discuss below.

3. Model C: Full capacitance matrix

In this subsection, we present our results for the capacitance matrix composed of all nonzero elements. In this case, the RK time-step calculation used was 0.05 for all the results in this section, with a current grid of $\delta i_{dc}/i_c = 0.005$. Except where otherwise noted, averaging was carried out over 6×10^4 time-steps and the first 2×10^4 were used for equilibration. Longer time-series have shown that while there are some long-lived transients, eventually the state becomes stable.

Since the off-diagonal matrix elements of $C_{\vec{r},\vec{r}'}$ decay algebraically, the definition of screening length as done in *Model B* does not strictly apply. Nonetheless, because of the specific decay in *Model C* we can still quantify the screening by the ratio of the off-diagonal capacitances to the diagonal ones, using the definition of *Model B*. We could have used another definition in which we sum over all the matrix elements, normalized appropriately, but the end result, that is the measure of screening, would be about the same. (In fact, we did just that, and found that while it resulted in a rescaling of the screening length by a small numerical factor, it did not change the qualitative behavior.)

Our results were obtained principally on an 8×8 array, but we have seen similar behavior in much larger arrays (e.g., 40×40). In this model, in contrast to *Model B*, we have seen only the $\frac{2}{7}$ -step which has to do with the nonzero decay of the off-diagonal matrix elements of the capacitance matrix. In *Model C* we can move con-

tinuously from *Model A* to *Model B* by adjusting two parameters: the self capacitance (by varying r_c) and the diameter of the disk, D , expressed in units of the lattice spacing. D takes values in the range $[0, 1]$, the upper limit giving *Model B* (or *Model A* if, in addition, $r_c = 0$). The lower limit corresponds to an array of superconducting dots which are too far separated for tunneling. As we decrease D from 1, for $\Lambda_0 \gg L_x$, a voltage step appears at $\langle V \rangle = \frac{2}{7}$, for $D = 0.997$, and disappears for $D = 0.95$. The results are shown in Fig. 12, for $\Lambda_0 = 32$ on an 8×8 array. The maximum width of the $\frac{2}{7}$ -step is of the same order of the half-step seen before¹⁰, though we chose $\beta_c = 0.5$ specifically to be outside the chaotic regime for which Hagaars *et al.*¹⁰ saw that step.

The magnitude of the step appears to be $\frac{2}{L_y-1}$, based on runs for $L_y = 4, 8$, and 16: that is, for each lattice size, we observe the appearance and subsequent disappearance of a step at $\langle V \rangle = \frac{2}{L_y-1}$ as D is varied down from 1. The occurrence of L_y in the expressions suggests that the GCFS are edge-like effects. They do not occur for *Model A*, but do occur for certain parameter values in *Model B*, as can be seen in Fig. 7. We also found qualitatively similar behavior (i.e., the existence of a step only for a limited range of $D \sim 1$) using the expression for the inverse capacitance matrix model of Whan *et al.*¹⁹

We have examined the width of the $\frac{2}{7}$ -step as a function of Λ_0 , as we fixed both $\nu = 0.1$ and $\beta_c = 0.5$. The results are shown in Fig. 13. There are some clear differences between the behaviors of *Models B* and *C*. We stress that because the screening in *Model B* is exponential for long and logarithmic for short distances, as compared to the algebraic decay in *Model C*, this is clearly seen in the different results in this figure.

The GCFS steps appear to be related to a partially screened phase-locked state. They do not appear to be metastable, in the sense that there is no need to ‘step’ up onto them, as was found in *Model B*. We also produced animations that show no stable vortex patterns, but indicate that all junctions in a transverse row evolve in phase without an apparent simple relationship between adjacent rows. We examined the voltage states of all junctions along the central column of the array (that is, the ladder consisting of all the junctions with $x = 4$), and found that there are essentially two kinds of behavior: The behavior of the edge junctions seems to be symmetrical about the line $y = L_y/2$, with their voltage (normalized for frequency) equal to unity. The other junctions, while not locked in or very much out of phase with each other, are in zero-voltage states. This is clearly due to screening.

We also looked at the spectral function of a *Model C* array. We find, sitting on the $\frac{2}{7}$ -step (having stepped up onto it), that when we study the spectra of the junctions within the center row, at one of the edges (all within the ladder defined by $x = 4$) or the whole array, all three cases show similar behavior.

There is a small but very long-lived transient, which

shows up in the power spectral density, as two peaks at frequencies approximately equal to $\sim \frac{4\nu}{7}$ and $\frac{5\nu}{7}$ (as shown in the inset of Fig. 14). Also present in the spectrum are the expected drive frequency $\nu = 0.1$, and its harmonics. We have verified that it *is* a transient and is not responsible for the appearance of the fractional steps, by allowing the array to equilibrate for very long periods of time. Under these conditions, we still see the step, and the power spectrum is very clean and shows no trace of the transient, as shown in the inset of Fig. 14.

Figure 14 shows the I-V's of an edge row of junctions, an interior row and the average of the whole array. Both edge rows behave similarly to each other, but differently from the interior rows. It is clear that the edge row enters a nonzero voltage state at a lower current than the interior row ($i_{dc} = 0.81$ *versus* $i_{dc} = 0.885$). That we have two out of seven rows in a voltage-producing state, and five out of seven in a zero-voltage state, seems to indicate that the $\frac{2}{7}$ -step has its origin not in a coherent oscillation of the array as a whole, but rather in the fact that some of the junctions get driven into a nonzero voltage state at a lower current than others, producing the observed $\frac{2}{7}$ -step. This is more easily seen in the 16×16 array, where multiple steps are visible. In particular, for $D = 0.999$, we see steps at $\frac{2}{15}$, $\frac{4}{15}$ and $\frac{6}{15}$. Looking at the I-V's for the individual rows, we can see first the outermost (edge) two rows (one at each boundary) switching on, followed by the next outermost rows, followed by the next outermost ones. The points where these rows sequentially switch on correspond to the beginning of a new step.

4. Size dependence

In the results reported above the size of the system appears prominently. The question is then how stable are these results as a function of lattice size and parameter values. Most of the results described in the previous sections have been generated in lattices of size $L_x = L_y = 8$. The steps we find are multiples of $\frac{1}{7}$ (since $L_y - 1 \equiv 7$). We also have looked at array sizes of $L_x = L_y = 16, 40$. In both cases, we found analogous GCFS at integer multiples of $\frac{1}{15}$ and $\frac{1}{39}$. In *Model B*, we notice that the maximum step width for the $\frac{1}{7}$ -step in the 8×8 array is about $\Delta i_{dc} = 0.10$, whereas for the 40×40 array, we find it to be ~ 0.085 . The widths are therefore comparable, and seem largely independent of lattice size. Figure 6 shows the I-V for a 40×40 array, with a screening length much smaller than the array ($\Lambda_0 = 1.75$).

In *Model B* we have examined the critical screening length Λ_0^{crit} for which the first step appears as a function of size L_x . We show in Fig. 15 the corresponding data, along with an approximate fit that gives $\Lambda_0^{\text{crit}} \sim L_x^{0.914 \pm 0.058}$. Figure 16 shows the maximum width of the first step as a function of L_x for a given maximum screening length Λ_0^{max} . Note that the first step is generally the biggest, regardless of lattice size. In addition, we show

in Fig. 17 that the maximal width of a step of a given order appears to saturate once the lattice size is above a certain minimum.

For *Model C*, we also investigated the size of the fractional steps as a function of the disk diameter, D . Figure 18 shows the dependence of the width of the $\frac{1}{15}$ -step in the 16×16 array. The qualitative behavior is very similar to that of the 8×8 array. Quantitatively, the difference lies in the values at which the steps appear and subsequently disappear. In the 8×8 array, the region of D -values for which the steps are visible is $D \in [0.950, 0.995]$, while in the 16×16 array, it is much smaller than that: $D \in [0.992, 0.9999]$.

IV. SUMMARY AND DISCUSSION

In this paper we have considered the general response of a Josephson-junction array that incorporates the capacitance matrix at different levels of approximation. We have considered three different models. *Model A* includes only the mutual capacitance between nearest-neighbor islands. This model has been studied to some extent before¹⁰. *Model B* includes the diagonal terms of $C_{\vec{r}, \vec{r}'}$ and had not been studied before. The important element in *Model B* is the *exponential* screening present at long distances that introduces important changes in the current response in the array: to wit, the new giant capacitive fractional steps (GCFS) that arise in the I-V's in this model, appearing and disappearing as the screening length Λ_0 changes. *Model C* incorporates the electrostatic interaction between all conducting islands. Since there is no exact solution known for an exact full capacitive matrix, we considered different model approximations to the full $C_{\vec{r}, \vec{r}'}$. Most of our results were based on an explicit solution for the capacitance of two disks of finite size in the plane using a superposition to construct the full matrix. This approach is similar to the one previously used in the full inductance-matrix problem¹³. We also used the numerically exact FASTCAP algorithm developed at MIT¹⁶. The essence and main result from all these calculations is that the full capacitance decays algebraically rather than exponentially as in *Model B*. We then concluded that the two-disk approximation contains, qualitatively at least, the essential properties of the full capacitance matrix of the more accurate problem.

Our results indicate that for screening lengths Λ_0 much larger than the lattice size, the I-V's display the characteristic giant Shapiro steps of the mutual capacitance model only (*Model A*¹⁰). That is, there are giant integer steps, and also (for certain values of β_c) the much smaller half-steps that are triggered by the onset of chaos in a single junction. The half-steps display the characteristic ACVS. The essential new result from our calculations in *Models B* and *C* is that there are new GCFS that essentially depend on the amount of screening in the model. The GCFS are not produced by oscillating vortices, as

in the non-full-capacitive problems, but are *localized* in restricted areas of the lattice due to electrostatic screening.

Generally, the size of the GCFS varies inversely with (though not necessarily proportionally to) the order: that is, lower-order steps are larger than higher-order ones. These fractional steps in *Model B* are metastable in nature, (that is, history-dependent but stable once produced) but remain for the longest runs we have carried out. Once $\Lambda_0 \sim 1$, all steps begin to disappear, and by $\Lambda_0 = 0.5$ they have completely vanished.

For *Model C* when $D = 1.0$ (and for large enough screening length, Λ_0), we have the under-damped results of *Model A*, and only see integer steps in the I-V's. As D decreases from 1.0, we enter a regime in which different rows have different values of i_{dc} at which they assume the coherent, nonzero voltage state. The rows closer to the boundaries of the array maintain the critical current of the under-damped array, while those towards the center become increasingly difficult to switch on. The interplay between the switching-on values for different rows determines the relative sizes of GCFS that we see. There may be no value of i_{dc} for which all the junctions in the array can oscillate in phase. This corresponds to both the shrinking of the integer steps, and the appearance of the fractional steps. As D decreases further, we enter a regime in which the coherent oscillation is no longer possible even for a single row. At this point, we have lost *all* the steps, fractional and otherwise.

The question naturally arises: To what extent does this behavior depend on the model used to construct the capacitance matrix? We believe this behavior to be independent of the model used, based on simulations we have carried out using results obtained independently, and by a completely different method by Whan *et al.*¹⁹ and the FASTCAP algorithm calculations. The idea now is to check the predictions of this paper experimentally.

ACKNOWLEDGMENTS

The authors would like to acknowledge fruitful discussions with Paul Tiesinga, Thomas Hagenars and Eugenio Ley-Koo. We thank J. White for telling us how to obtain FASTCAP. This work was supported in part by NSF grants DMR-95-21845 and DMR-9821845.

APPENDIX: A

In this appendix, we describe how to obtain the capacitance of two disks given in Eqs. (4) and (5) used in the array calculations. It is best to use bipolar coordinates (see Ref. 20) to obtain the relevant expression but then we shall transform to Cartesian coordinates as used in the calculations^{14,15}. These coordinates are related to the Cartesian coordinates through the equations

$$x = \frac{a \sinh \eta}{(\cosh \eta - \cos \xi)}, \quad y = \frac{a \sin \xi}{(\cosh \eta - \cos \xi)}, \quad z = z. \quad (A1)$$

The parameter η measures the diameter of the disks. $\eta = -\infty$ represents an infinitesimally small disk at position $(-a, 0)$. As η increases, the disk grows becoming infinite in size, at $\eta = 0$. Increasing η further causes the disk to shrink until it becomes a point at $(a, 0)$, for $\eta = +\infty$. The parameter a denotes the distance of the points $\eta = \pm\infty$ from the y -axis, $a \coth \eta$ is the distance from the center of the disks to the y -axis, i.e., half of the separation distance between the centers of the disks. The lines of constant η represent the boundaries of the disks.

The orthogonality of the bipolar coordinates can be established by evaluating the infinitesimal displacement from Eq. (A1) and identifying the respective scale factors and unit vectors:

$$\begin{aligned} d\vec{r} &= \hat{e}_x dx + \hat{e}_y dy + \hat{e}_z dz = \hat{e}_\xi h_\xi d\xi + \hat{e}_\eta h_\eta d\eta + \hat{e}_z h_z dz, \\ h_\xi &= h_\eta = \frac{a}{\cosh \eta - \cos \xi}, \quad h_z = 1, \\ \hat{e}_\xi &= \frac{-\hat{e}_x \sinh \eta \sin \xi + \hat{e}_y (\cosh \eta \cos \xi - 1)}{\cosh \eta - \cos \xi}, \\ \hat{e}_\eta &= \frac{-\hat{e}_x (\cosh \eta \cos \xi - 1) - \hat{e}_y \sinh \eta \sin \xi}{\cosh \eta - \cos \xi}. \end{aligned}$$

The electrostatic potential function between the two disks satisfies the Laplace equation, so from the previous equations we get,

$$\frac{1}{h_\xi h_\eta} \left[\frac{\partial^2}{\partial \xi^2} + \frac{\partial^2}{\partial \eta^2} \right] \phi(\xi, \eta) = 0. \quad (A2)$$

The general solution to Eq. (A2) can be written as

$$\begin{aligned} \phi(\xi, \eta) &= \sum_{m=0}^{\infty} [A_m \cos(m\xi) + B_m \sin(m\xi)] \\ &\quad \times [C_m \cosh(m\eta) + D_m \sinh(m\eta)]. \end{aligned} \quad (A3)$$

Taking the disks with centers at $\eta = \eta_1$ and $\eta = \eta_2$, the boundary conditions are $\phi(\xi, \eta = \eta_1) = V_1$, and $\phi(\xi, \eta = \eta_2) = V_2 = 0$. To get the electrostatic potential function we only need the case $m = 0$:

$$\phi(\xi, \eta) = \frac{V_2(\eta - \eta_1) + V_1(\eta_2 - \eta)}{\eta_2 - \eta_1}. \quad (A4)$$

The electric field intensity is obtained by taking the negative gradient of Eq. (A4), and only has \hat{e}_η -direction components:

$$\vec{E} = -\vec{\nabla} \phi = -\frac{V_2 - V_1}{h_\eta(\eta_2 - \eta_1)} \hat{e}_\eta. \quad (A5)$$

The electric charge distribution on each of the disks is given by

$$\begin{aligned}\sigma(\xi, \eta = \eta_1) &= \frac{\hat{e}_\eta \cdot \vec{E}}{4\pi} \Big|_{\eta=\eta_1} \\ &= -\frac{(V_2 - V_1)(\cosh \eta_1 - \cos \xi)}{4\pi(\eta_2 - \eta_1)a}, \\ \sigma(\xi, \eta = \eta_2) &= -\frac{\hat{e}_\eta \cdot \vec{E}}{4\pi} \Big|_{\eta=\eta_2} \\ &= \frac{(V_2 - V_1)(\cosh \eta_2 - \cos \xi)}{4\pi(\eta_2 - \eta_1)a}.\end{aligned}\quad (\text{A6})$$

The total charges are obtained by integrating Eqs. (A6) over the respective disks

$$\begin{aligned}Q_1 &= \int_0^h \int_0^{2\pi} \sigma(\xi, \eta = \eta_1) h_\xi d\xi dz \\ &= -\frac{V_2 - V_1}{4\pi(\eta_2 - \eta_1)} 2\pi h = -\frac{V_2 - V_1}{2(\eta_2 - \eta_1)} h.\end{aligned}\quad (\text{A7})$$

Therefore the capacitance of the bipolar capacitor with height h , follows from Eq. (A7),

$$C = \frac{Q_1}{(V_1 - V_2)h} = \frac{1}{2(\eta_2 - \eta_1)}. \quad (\text{A8})$$

Now to use this result in our calculations we need to transform it appropriately to the lattice structure of the square lattices considered in this paper. Eq. (A8) assumes that the two disks are different. In the arrays we have studied the disks have the same radius and thus $\eta_1 = \eta$ and $\eta_2 = -\eta_1 = -\eta$, so that the capacitance of the two disks is

$$C = \frac{1}{4\eta}. \quad (\text{A9})$$

Now going back to Cartesian coordinates, we can express η and ξ as follows:

$$\eta = \tanh^{-1} \left[\frac{2ax}{a^2 + x^2 + y^2} \right], \quad (\text{A10})$$

$$\xi = \tanh^{-1} \left[\frac{2ax}{a^2 - x^2 - y^2} \right]. \quad (\text{A11})$$

We define d as the ratio of the radius of the disk to the distance of its center from the origin (or, equivalently, the ratio of the diameter to the distance between the centers of two adjacent disks):

$$d = \frac{a|\text{csch } \eta|}{a \coth \eta} = \frac{1}{\cosh \eta}. \quad (\text{A12})$$

This provides a way to parameterize the separation between adjacent disks. Since $\cosh x \equiv (e^x + e^{-x})/2 \geq 1, \forall x$, d lies in the range $[0, 1)$. When $d \lesssim 1$, the disks are almost touching, and each disk occupies almost all of the lattice unit cell. We expect this to correspond to *Model A*. When $d \simeq 0$, then the disks are separated by a very large distance in relation to their diameter. This

scenario corresponds to weak screening. We will express the capacitance in terms of this d parameter.

Taking $y = 0$, and measuring distances in units of a hereafter, Eq. (A10) becomes

$$\eta = \tanh^{-1} \left[\frac{2x}{1 + x^2} \right]. \quad (\text{A13})$$

The points where the disk intersects with the x -axis are given by $(x - \coth \eta)^2 = \text{csch}^2 \eta$ (the equation of a circle of radius $\text{csch} \eta$, centered at $\coth \eta$). This has solutions $x = (\cosh \eta \pm 1)/\sinh \eta$, which can be expressed in terms of d :

$$x = \frac{1 \pm d}{\sqrt{1 - d^2}} \quad (\text{A14})$$

(There are two values of x for each d —each gives the same expression for the capacitance, as it should.) Plugging the solutions in Eq. (A14) into Eq. (A13) gives us:

$$\begin{aligned}\eta &= \tanh^{-1} \left[\frac{2(1 \pm d)}{\sqrt{1 - d^2}} \frac{1 - d^2}{1 - d^2 + (1 \pm d)^2} \right] \\ &= \tanh^{-1} \left[\sqrt{1 - d^2} \right].\end{aligned}\quad (\text{A15})$$

Therefore, the capacitance behaves as:

$$C = \frac{1}{4 \tanh^{-1} [\sqrt{1 - d^2}]}, \quad (\text{A16})$$

where d is the ratio of the disk diameter to the distance between the centers of two adjacent disks. This is the result used in our calculations and given in Eqs. (4) and (5).

As a check on this result, we can look at the behavior as $d \rightarrow 0$. This problem has been solved by Jackson¹⁴ (problem 1.7, p. 51) who gives the capacitance per unit length for a pair of infinite parallel wires, with a ratio of radius to separation $d \ll 1$, as $C = -1/4\ell n d$.

By using the expression²¹:

$$\tanh^{-1} z = \frac{1}{2} \ell n \left[\frac{1+z}{1-z} \right],$$

and expanding binomially the square root of Eq. (A15) in the limit of small d , we find that

$$\tanh^{-1} \left[\sqrt{1 - d^2} \right] \rightarrow \frac{1}{2} \ell n \left(\frac{4}{d^2} \right) = \ell n (2/d) \simeq -\ell n d. \quad (\text{A17})$$

This gives us

$$C(d)_{d \rightarrow 0} \simeq \frac{-1}{4\ell n d}. \quad (\text{A18})$$

Thus, we have agreement between our model and a known solution in the limit of small d .

* Permanent address.

- ¹ For a review of superconducting networks see *Proceedings of the 2nd CTP Workshop on Statistical Physics: KT Transition and Superconducting Arrays*, edited by D. Kim, J. S. Chung and M. Y. Choi (Min Eum Sa, Seoul, 1993). *Macroscopic quantum phenomena and coherence in superconducting networks*, edited by C. Giovannella and M. Tinkham. (World Scientific, Singapore, 1995).
- ² D. Domínguez and J. V. José, Phys. Rev. Lett. **69**, 414 (1992).
- ³ J. R. Phillips, H. S. J. van der Zant, J. White, and T. P. Orlando, Phys. Rev. B **47**, 5219 (1993).
- ⁴ S. G. Lachenmann *et al.*, Phys. Rev. B **56**, 5564 (1997).
- ⁵ T. D. Clark, Phys. Rev. B **8**, 137 (1973).
- ⁶ S. P. Benz, M. S. Rzchowski, M. Tinkham, and C. J. Lobb, Phys. Rev. Lett. **64**, 693 (1990).
- ⁷ K. H. Lee, D. Stroud, and J. S. Chung, Phys. Rev. Lett. **64**, 692 (1990); K. H. Lee and D. Stroud, Phys. Rev. B **43**, 5280 (1991).
- ⁸ J. U. Free *et al.*, Phys. Rev. B **41**, 7267 (1990); M. Octavio *et al.*, *ibid.* **44**, 4601 (1991).
- ⁹ D. Domínguez, J. V. José, A. Karma, and C. Wiecko, Phys. Rev. Lett. **67**, 2367 (1991); D. Domínguez and J. V. José, Phys. Rev. B **48**, 13717 (1993).
- ¹⁰ T. J. Hagenaars, Jorge V. José, J. E. van Himbergen, and P. H. E. Tiesinga (submitted); T. J. Hagenaars, Ph. D. thesis, Utrecht University, 1995.
- ¹¹ J. E. Mooij, B. J. van Wees, and L. J. Geerligs, Phys. Rev. Lett. **65**, 645 (1990).
- ¹² S. P. Benz and C. J. Burroughs, Supercond. Sci. Tech. **4**, 561 (1991); P. A. A. Booij and S. P. Benz, Appl. Phys. Lett. **64**, 2163 (1994).
- ¹³ D. Domínguez and J. V. José, Int. J. Mod. Phys. B **8**, 3749 (1994); D. Domínguez and J. V. José, Phys. Rev. B **53**, 11692 (1996).
- ¹⁴ J. D. Jackson, *Classical Electrodynamics*. Second Edition (John Wiley, New York, 1975).
- ¹⁵ E. Ley-Koo and G. Monsivais, Rev. Mex. Phys. **41**, 610 (1995); A. Góngora-T and E. Ley-Koo *ibid.* **42**, 663 (1996).
- ¹⁶ K. Nabors, S. Kim, and J. White, IEEE Trans. Microwave Theory Tech. **40**, 1496 (1992).
- ¹⁷ H. S. J. van der Zant *et al.*, Phys. Rev. B **38**, 5154 (1988); T. S. Tighe, A. T. Johnson, and M. Tinkham, Phys. Rev. B **44**, 10286 (1991); H. S. J. van der Zant, Ph.D. thesis, Technische Universiteit Delft, 1988.
- ¹⁸ W. H. Press, B. P. Flannery, S. A. Teukolsky, and W. T. Vetterling, *Numerical Recipes: The Art of Scientific Computing*, (Cambridge University Press, Cambridge, UK, 1989).
- ¹⁹ C. B. Whan, J. White, and T. P. Orlando, Appl. Phys. Lett. **68**, 2996 (1996).
- ²⁰ G. B. Arfken and H. J. Weber, *Mathematical methods for physicists*. Fourth edition (Academic Press, San Diego, 1995)
- ²¹ I. S. Gradshteyn and I. M. Ryzhik, edited by Alan Jeffrey. Fifth edition (Academic Press, Boston, 1994)

FIG. 1. Diagram of the array studied. The symbols \boxtimes denote the capacitive junctions. Current is injected from the bottom, and extracted from the top, with periodic boundary conditions along the direction perpendicular to the current flow.

FIG. 2. This figure illustrates the two-disk model. D is their diameter *measured in units of the lattice spacing* and R the separation distance between them. When $D \lesssim 1$, the array is close-packed, with D almost equal to the lattice spacing. When $D \ll 1$, the array is loosely packed, with the disks widely spaced from each other, and thus no current can flow between them. Our model is not valid for this value of $D \ll 1$.

FIG. 3. Comparison of behavior of capacitances for different model calculations. The lines represent the following models: FASTCAP calculation (---); *Model C* two-disk approximation (—) for $D = 0.99$, and (—) for $D = 0.1$; finite-potential disk embedded in an infinite zero-potential conducting plane (—). The inset shows the conductor plate array used in the FASTCAP calculations. The plates are of side ℓ , with thicknesses ranging from 1000 to 35000 Å.

FIG. 4. *Model C* I-V's for a DC-driven array, as a function of D , for an 8×8 array. The solid line was obtained with $D = 0.20$, the dashed one with $D = 0.99999$. $\beta_c = 0.50$.

FIG. 5. FASTCAP model I-V's for a DC-driven array, as a function of the ratio of the diameter \tilde{D} to the lattice spacing for an 8×8 array studied by Whan *et al.*[19]. The solid line was obtained with $\tilde{D} = 0.050$, the dashed one with $\tilde{D} = 0.970$. Parameter values are $\beta_c = 0.50$. We use a different diameter value than in the two-disk case since they are not exactly the same.

FIG. 6. *Model B* I-V curves for a 40×40 array illustrating the GCFS of decreasing size and visible at $\frac{1}{39}, \frac{2}{39}, \frac{3}{39}, \frac{4}{39}$ (just). The inset shows the same steps, with the y -coordinate multiplied by 39 to show the precise values of the steps. $\beta_c = 0.50, \nu = 0.10, \Lambda_0 = 1.75$. The Λ_0 value chosen corresponds to one chosen in previous figures.

FIG. 7. Four I-V's for *Model B*, corresponding to $\Lambda_0 = 32, 8, 3, 1.75$, from left to right, and each displaced for clarity successively by 0.5 units to the right. They show how the integer $n = 1$ step is rapidly destroyed as Λ_0 , is reduced below the array size ($L_x = 16, L_y = 16$). Just as the integer step disappears, a fractional step emerges (a central subject of this paper). Parameter values are $\beta_c = 0.5, \nu = 0.1$, and $i_{ac} = 1.0$.

FIG. 8. The $n = 1$ step width is shown as a function of Λ_0 , for *Model B*. It is clear that once the screening length becomes less than half the array size ($L_x = L_y = 16$), the step is destroyed. Values for β_c , ν , and i_{ac} are the same as in Fig. 7.

FIG. 9. The width of the fractional $\frac{2}{7}$ -step is shown as a function of ν , in *Model B*. Values for β_c , i_{ac} are the same as in Fig. 7 and $\Lambda_0 = 1.75$. Not shown are values of $\nu \in [0.3, 0.6]$, for which we have verified that there is no step.

FIG. 10. The widths of the $\frac{1}{7}$ -, $\frac{2}{7}$ -, and $\frac{3}{7}$ -steps (symbols \blacktriangle , \blacksquare and \blacklozenge respectively) as a function of β_c , in *Model B*. Parameter values for ν , and Λ_0 are the same as in Fig. 7. We have also looked for (but not found) other steps but did not find them for $\beta_c \leq 10.0$.

FIG. 11. *Model B* widths of the $\frac{1}{7}$ - and $\frac{2}{7}$ -steps (symbols \bullet and \blacktriangle respectively) shown as functions of Λ_0 . Values for β_c and ν are the same as in Fig. 7. We also have looked for other steps for all values of $\Lambda_0 \leq 32$. The inset shows an I-V showing the hysteresis of the fractional steps in *Model B*. The dashed (solid) line indicates data taken as the current is increased (decreased), as shown by the arrows. Here $\beta_c = 0.50$, $\nu = 0.10$, $\Lambda_0 = 1.75$, $\delta i_{dc} = 0.005$.

FIG. 12. The width of the $\frac{2}{7}$ -step as a function of the diameter, D , in *Model C*. See Fig. 2 for an explanation of the symbol D . $\beta_c = 0.5$, $\nu = 0.1$. Note that the step exists only for a small range of D -values.

FIG. 13. The width of the $\frac{2}{7}$ -step (\bullet) as a function of Λ_0 , for *Model C* with $D = 0.994$ (this value gives the maximum step-width for $\Lambda_0 = 5.66$). The step-width in *Model B* is shown for comparison (\blacklozenge). $\beta_c = 0.50$, $\nu = 0.10$, $L_x = L_y = 8$.

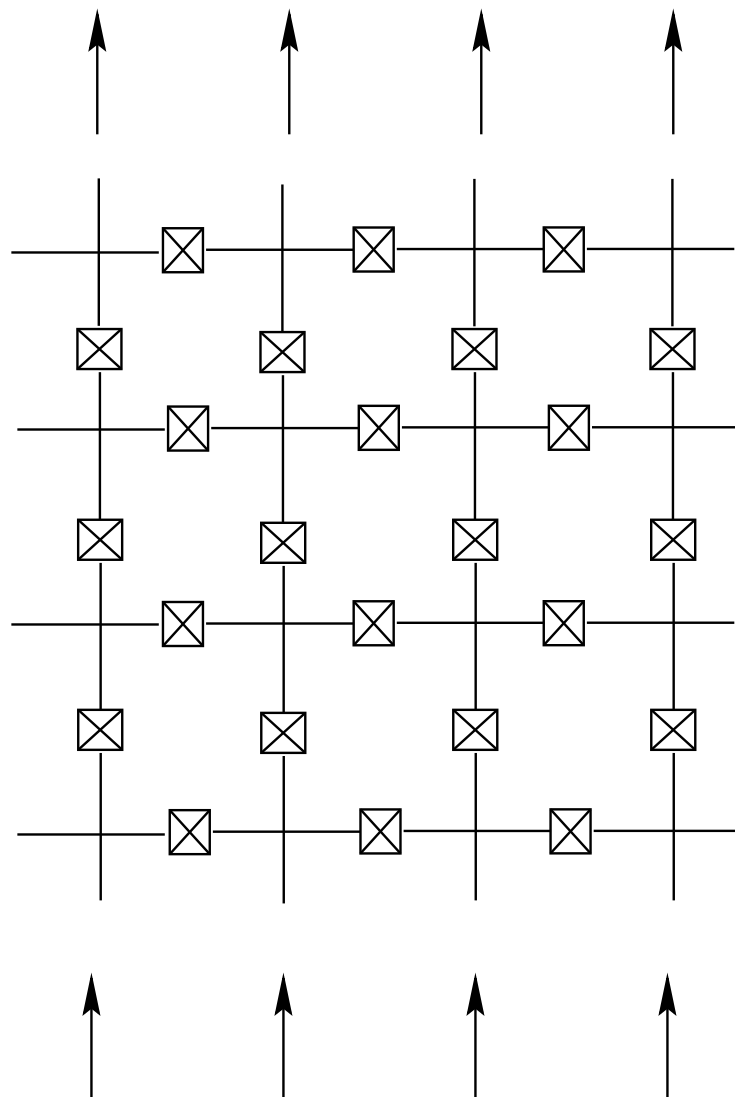
FIG. 14. *Model C* I-V's for individual rows of array showing $\frac{2}{7}$ -step. The solid line represents the array average, the dashed line represents the edge junctions, while the dashed-dotted line represents interior junctions. Parameter values are $\beta_c = 0.50$, $\nu = 0.10$. The inset shows the power spectrum for the $\frac{1}{7}$ -step in *Model B*. Parameter values are $\beta_c = 0.50$, $\nu = 0.10$. The drive frequency and harmonics are clearly visible, as are other peaks at roughly $\frac{4\nu}{7}$ and $\frac{5\nu}{7}$. We have verified that these latter are transients.

FIG. 15. This figure shows the minimum value of the screening length Λ_0 , as a function of L_x , for which the first step is visible, in *Model B*. The data points are shown as \bullet , fitted to the dashed line by $\log \Lambda_0 \sim \log L_x^{0.914 \pm 0.058}$. Values for β_c , and ν are as shown in Fig. 7.

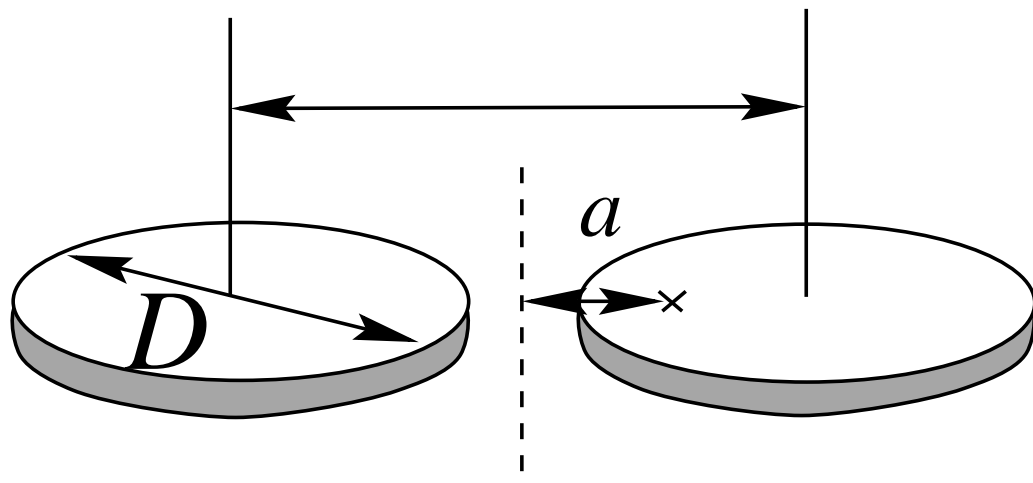
FIG. 16. We show, as a function of L_x in *Model B*, the value of the screening length which maximizes the width of the fractional steps. β_c , i_{ac} , and ν are as in Fig. 7. The line is simply a guide to the eye.

FIG. 17. The maximal width Δi_{dc}^{\max} of the fractional steps in *Model B*, is shown as a function of lattice size. The symbols \bullet , \blacksquare , \blacklozenge represent the first through third steps respectively (i.e., $\frac{1}{L_x-1}$, $\frac{2}{L_x-1}$, $\frac{3}{L_x-1}$ etc.). (Not all steps can be obtained for all lattice sizes.) This step-width appears to saturate, though not at the same lattice size for all steps.

FIG. 18. Step width Δi_{dc} as a function of disk diameter, D , in *Model C* for a 16×16 array. Data are for $\frac{2}{15}$ -step (the lowest-order step seen). Parameter values are $\beta_c = 0.50$, $\nu = 0.10$.

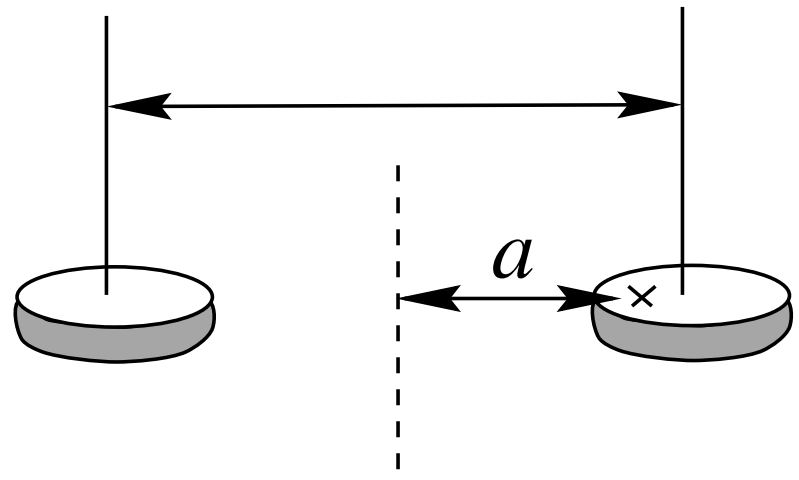
I_{ext}  I_{ext}

$$R = 2a \coth \eta$$

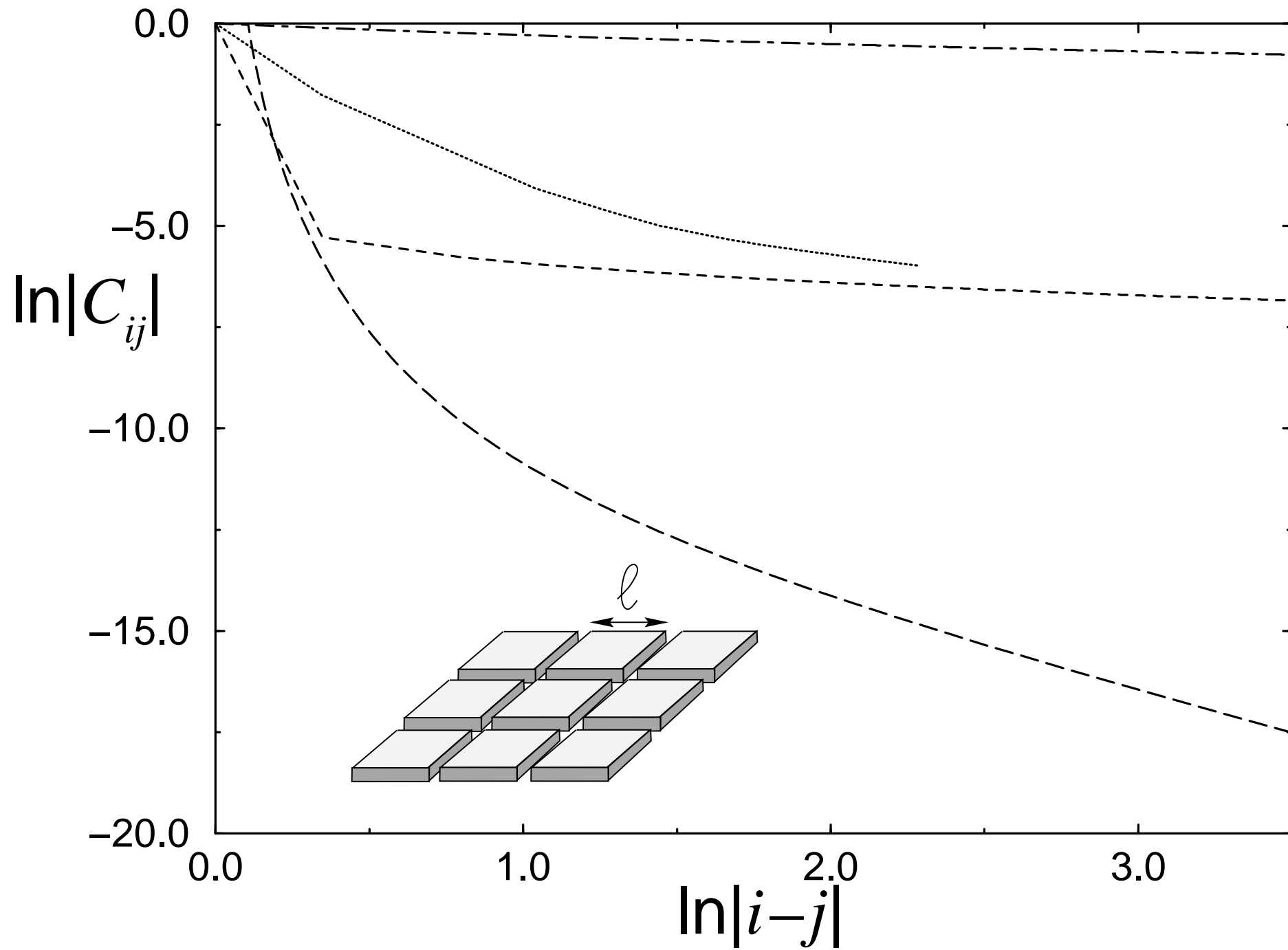


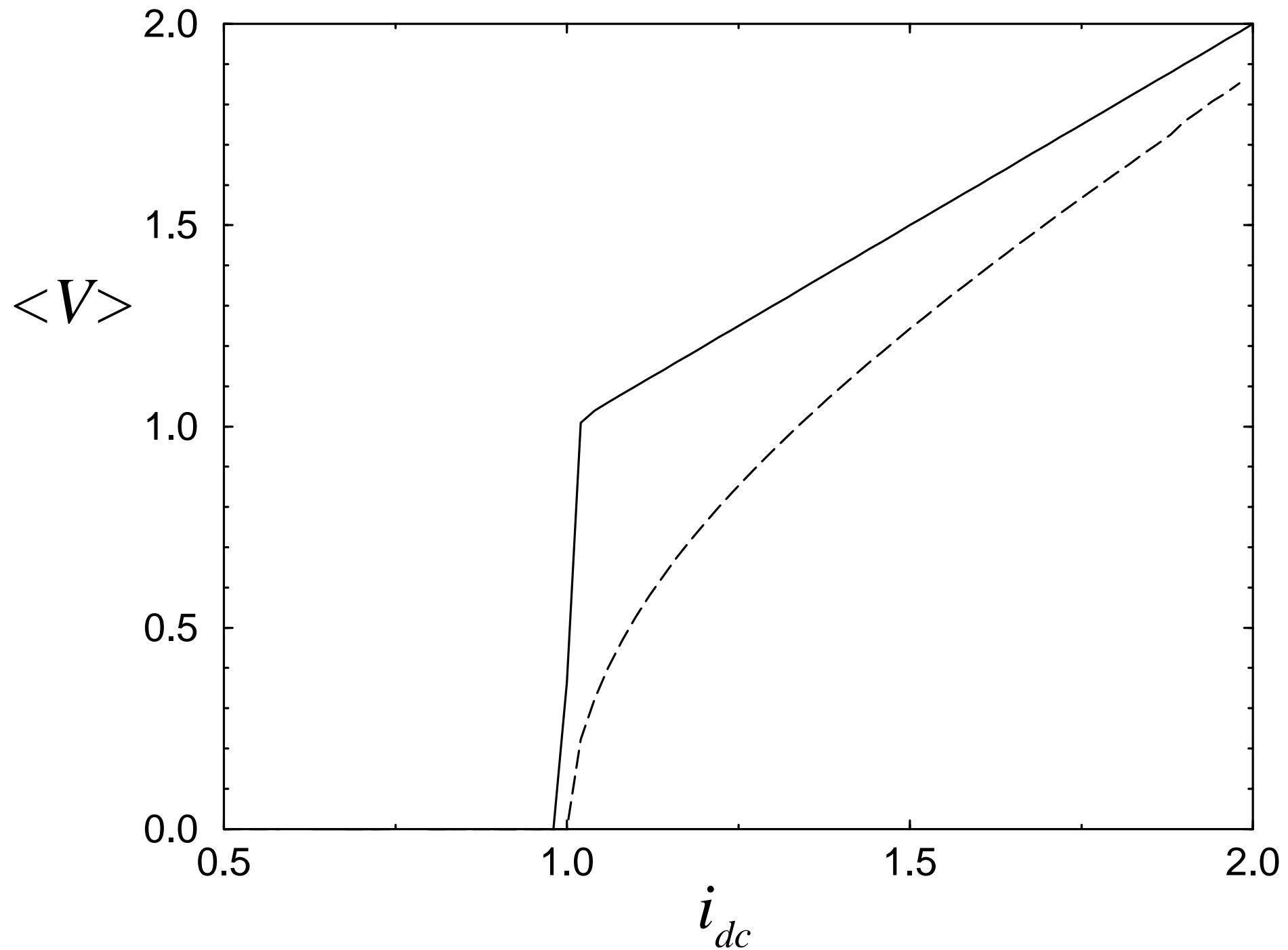
$$D/R \sim 1.0$$

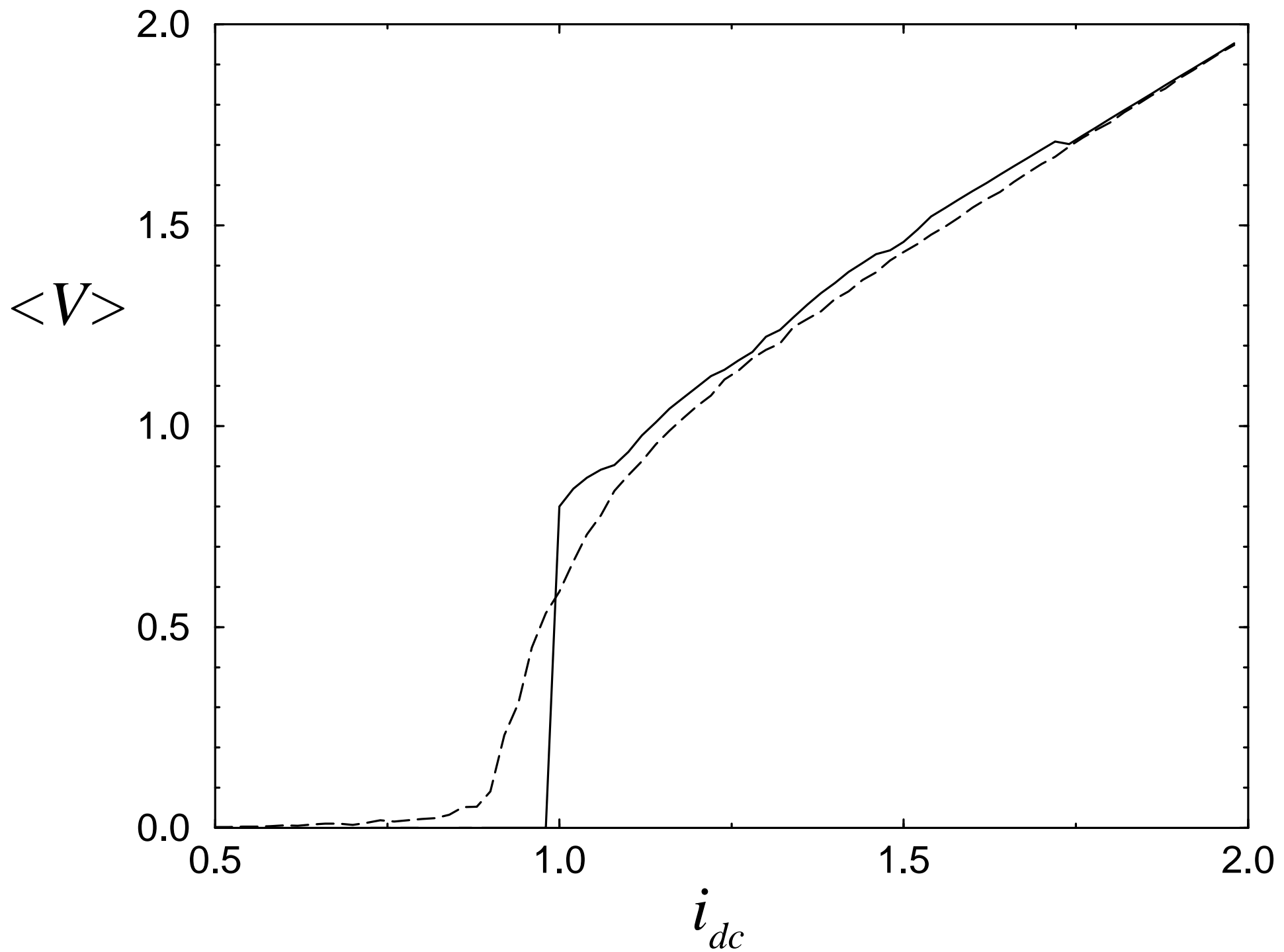
$$R = 2a \coth \eta$$

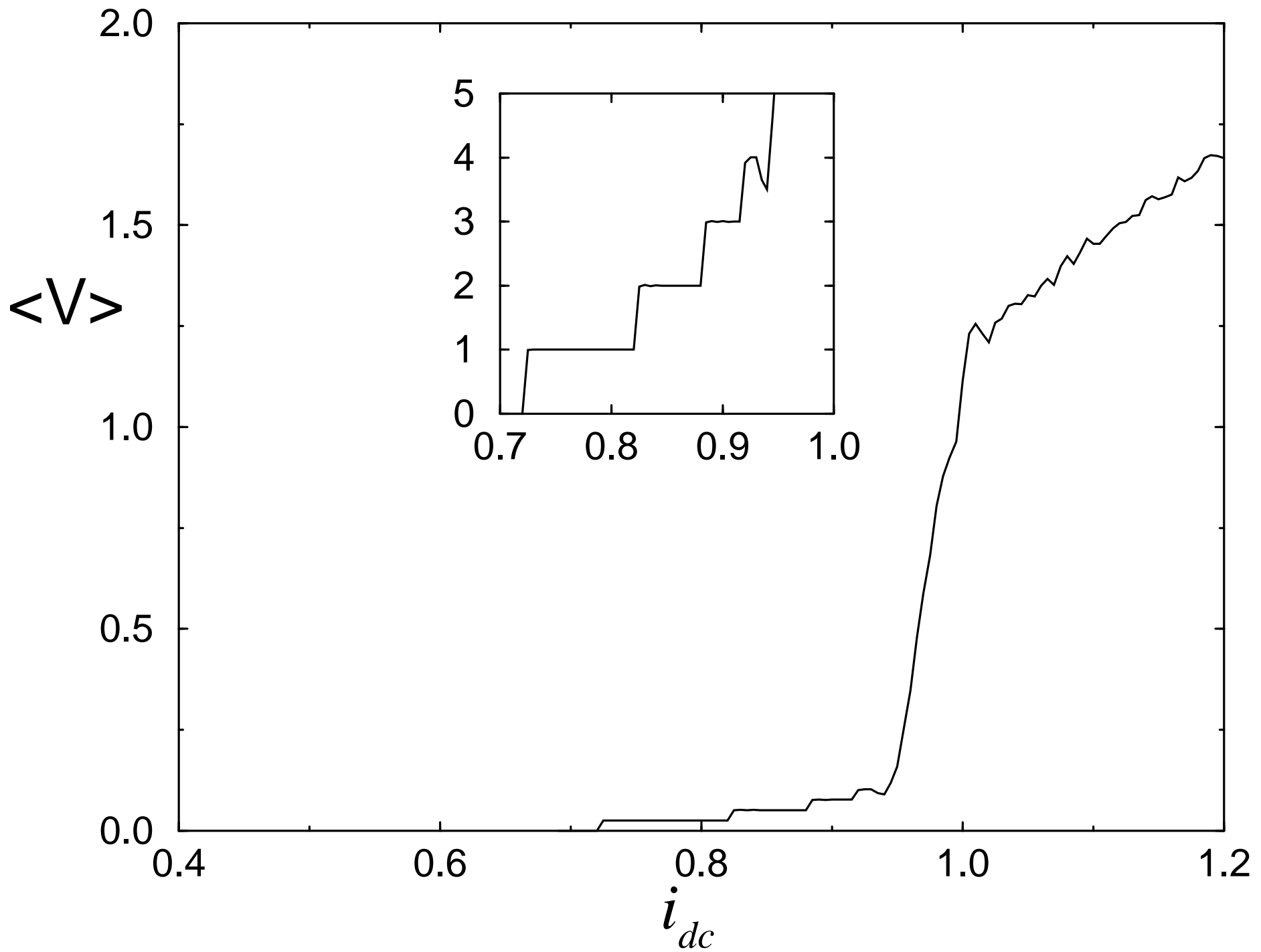


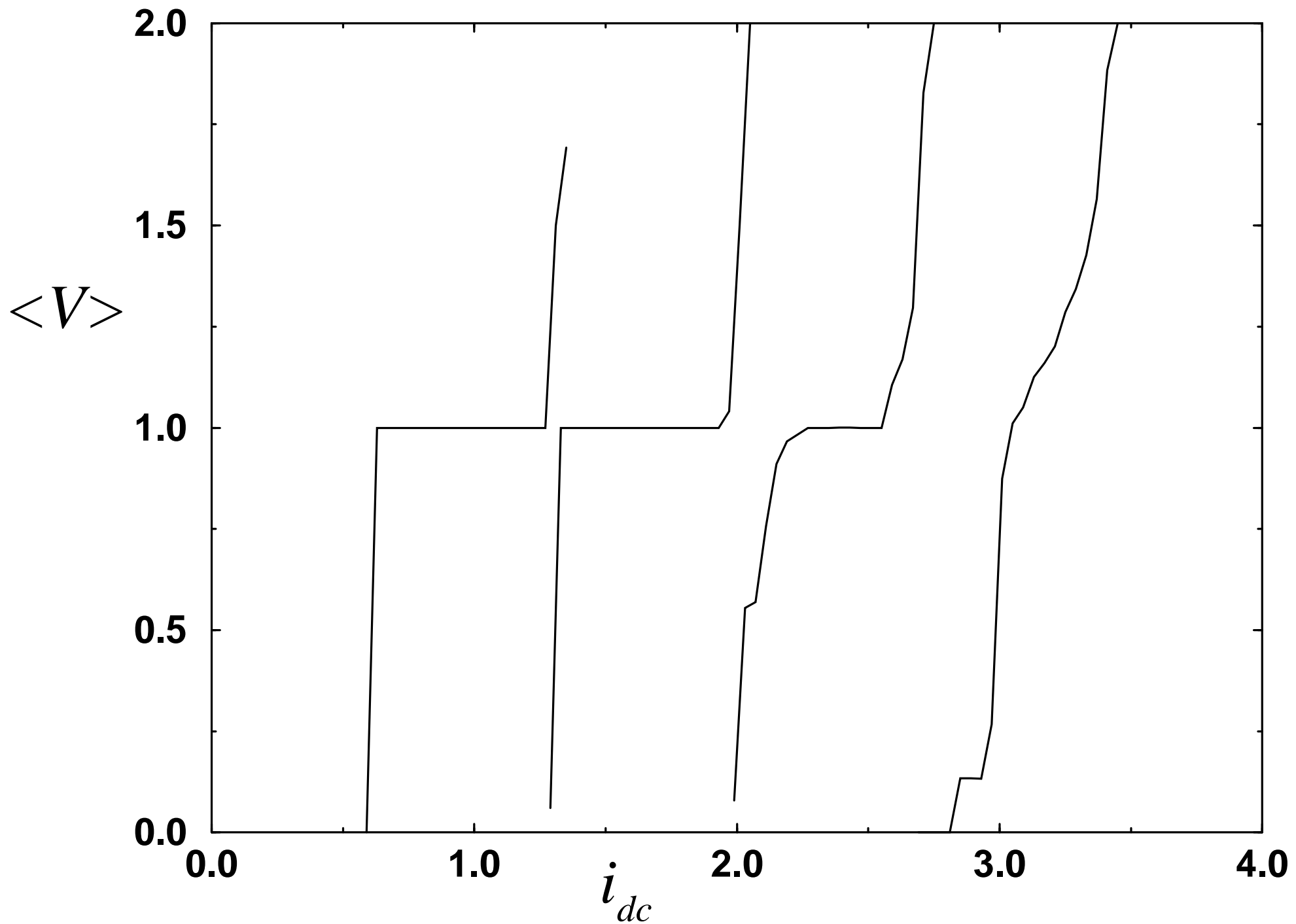
$$D/R \ll 1.0$$

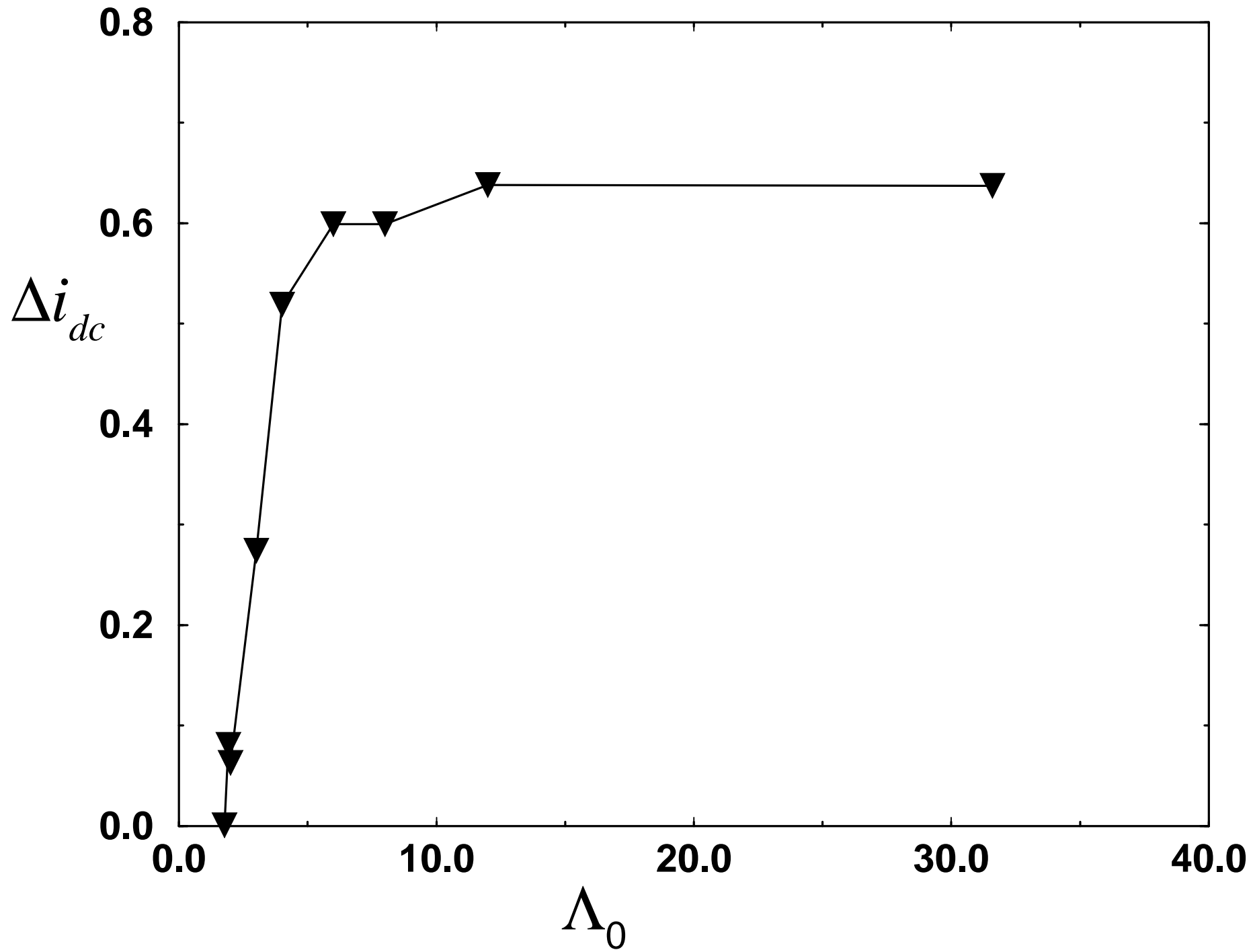


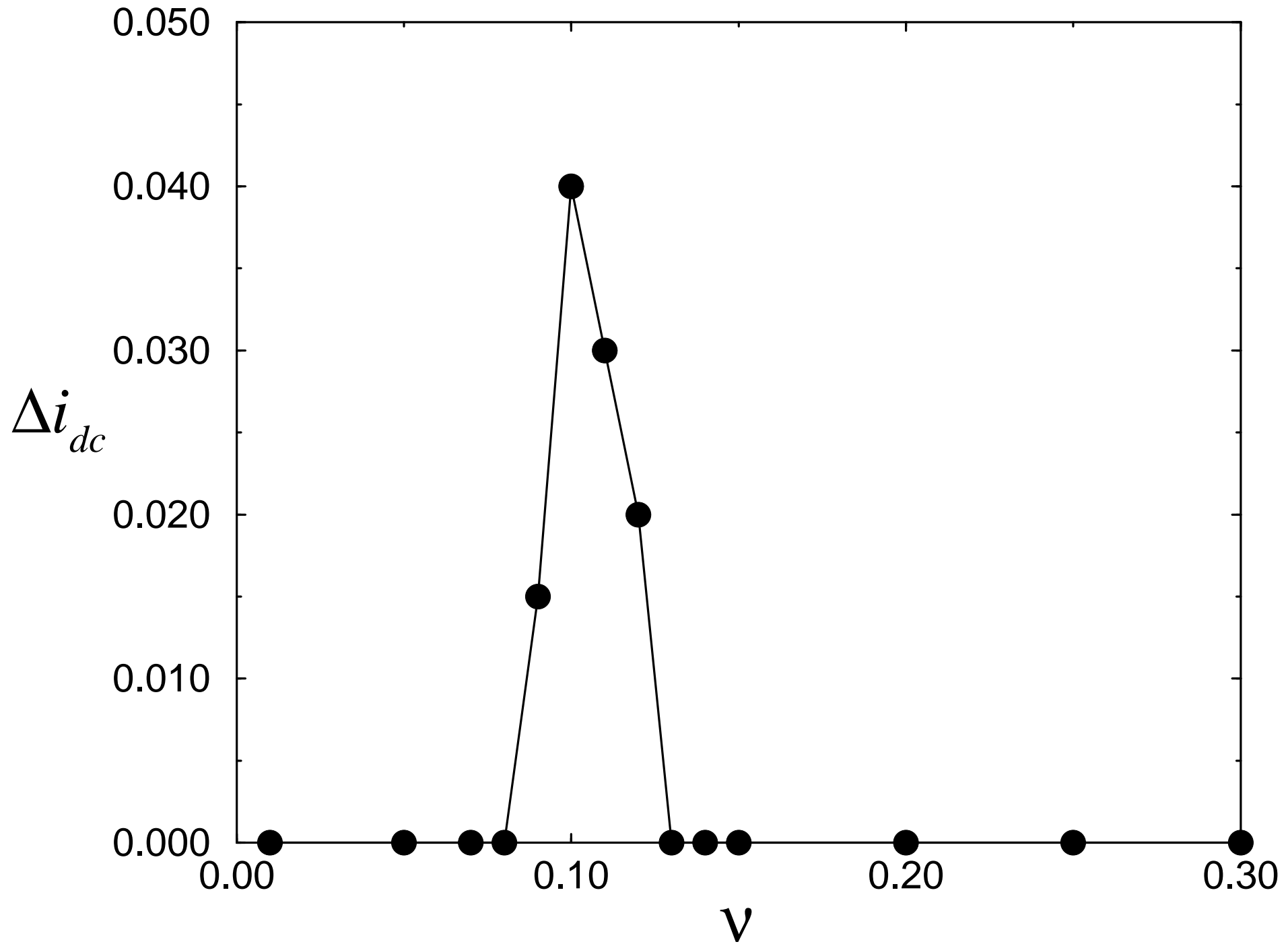


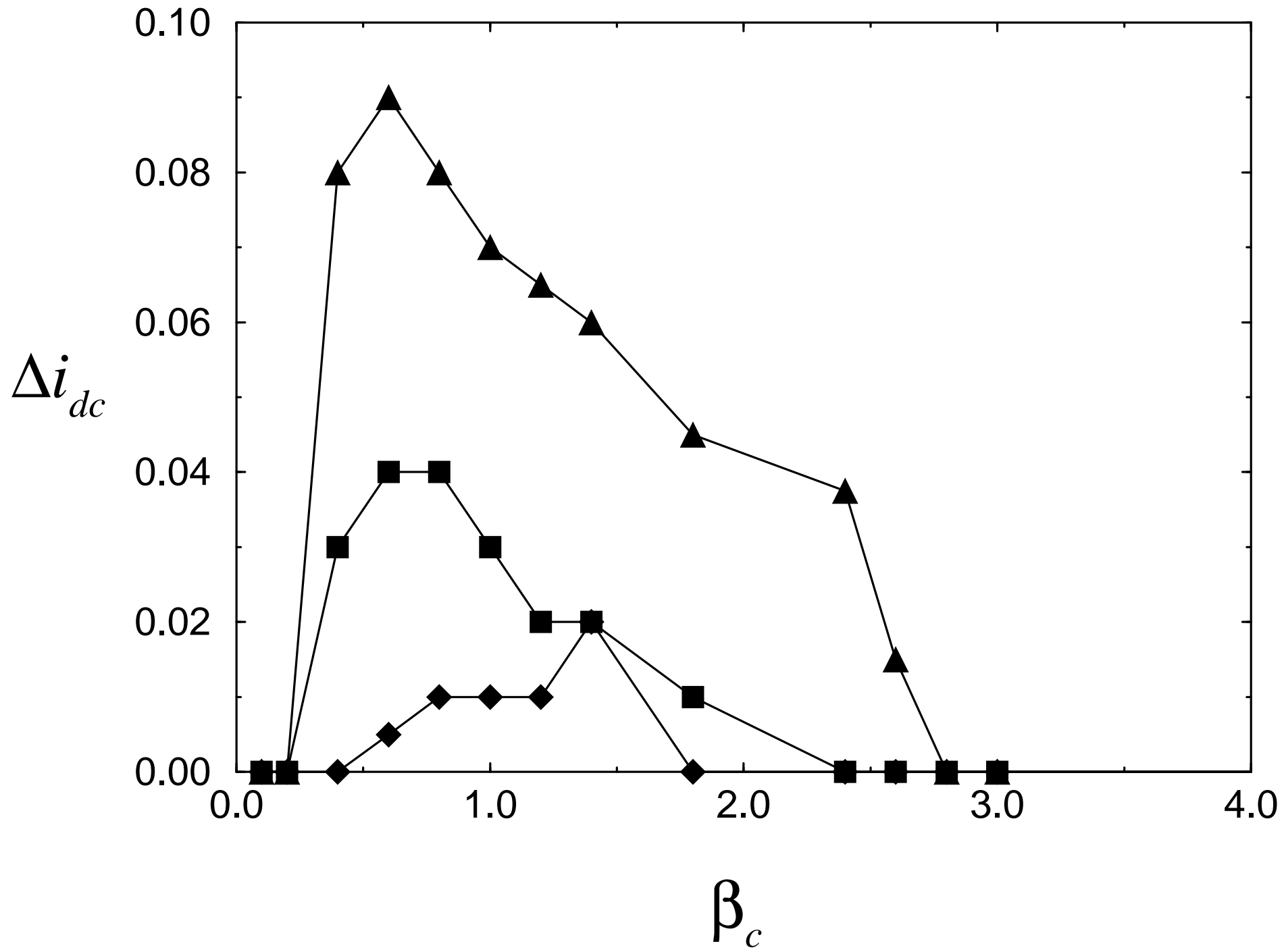


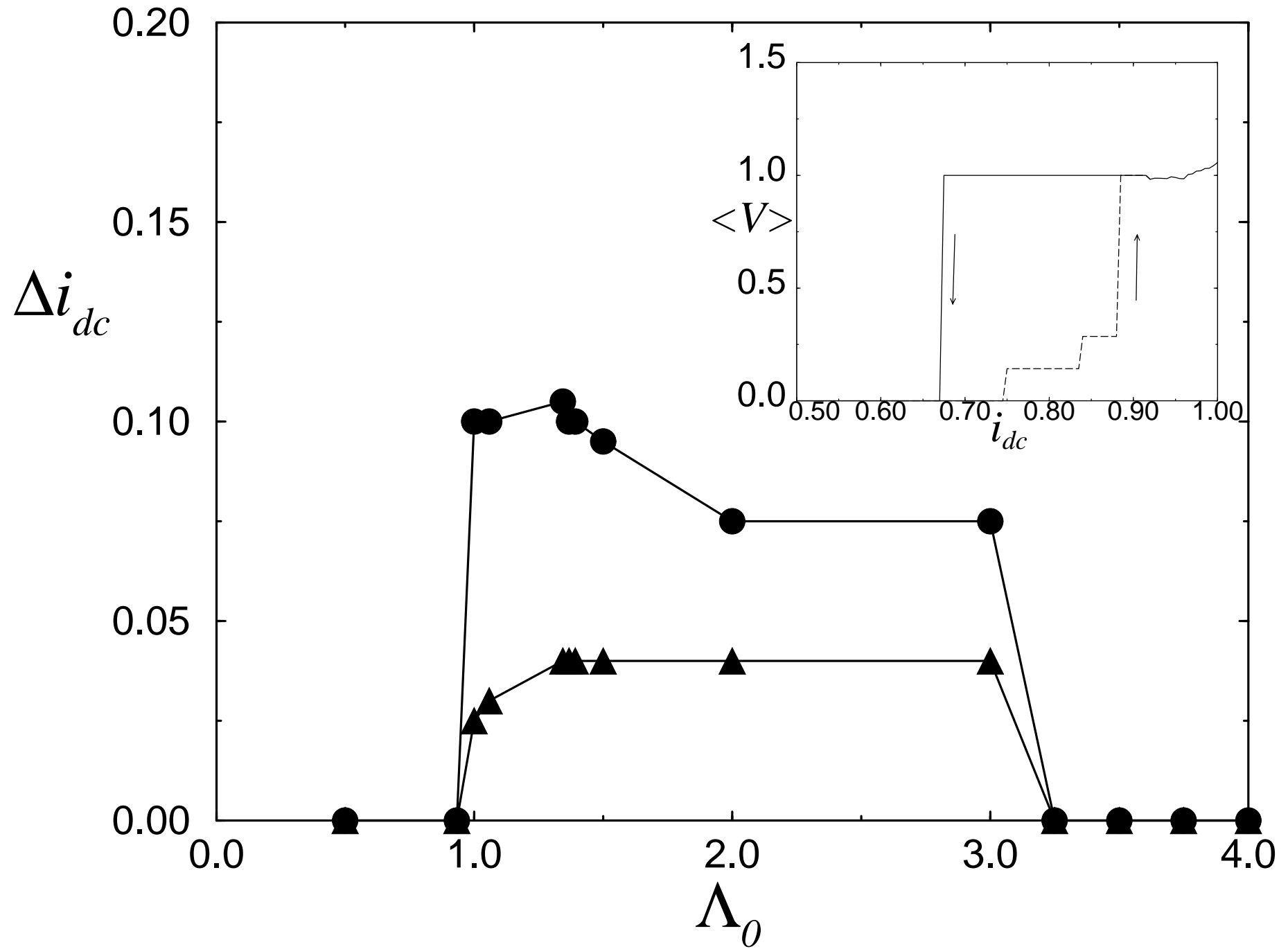


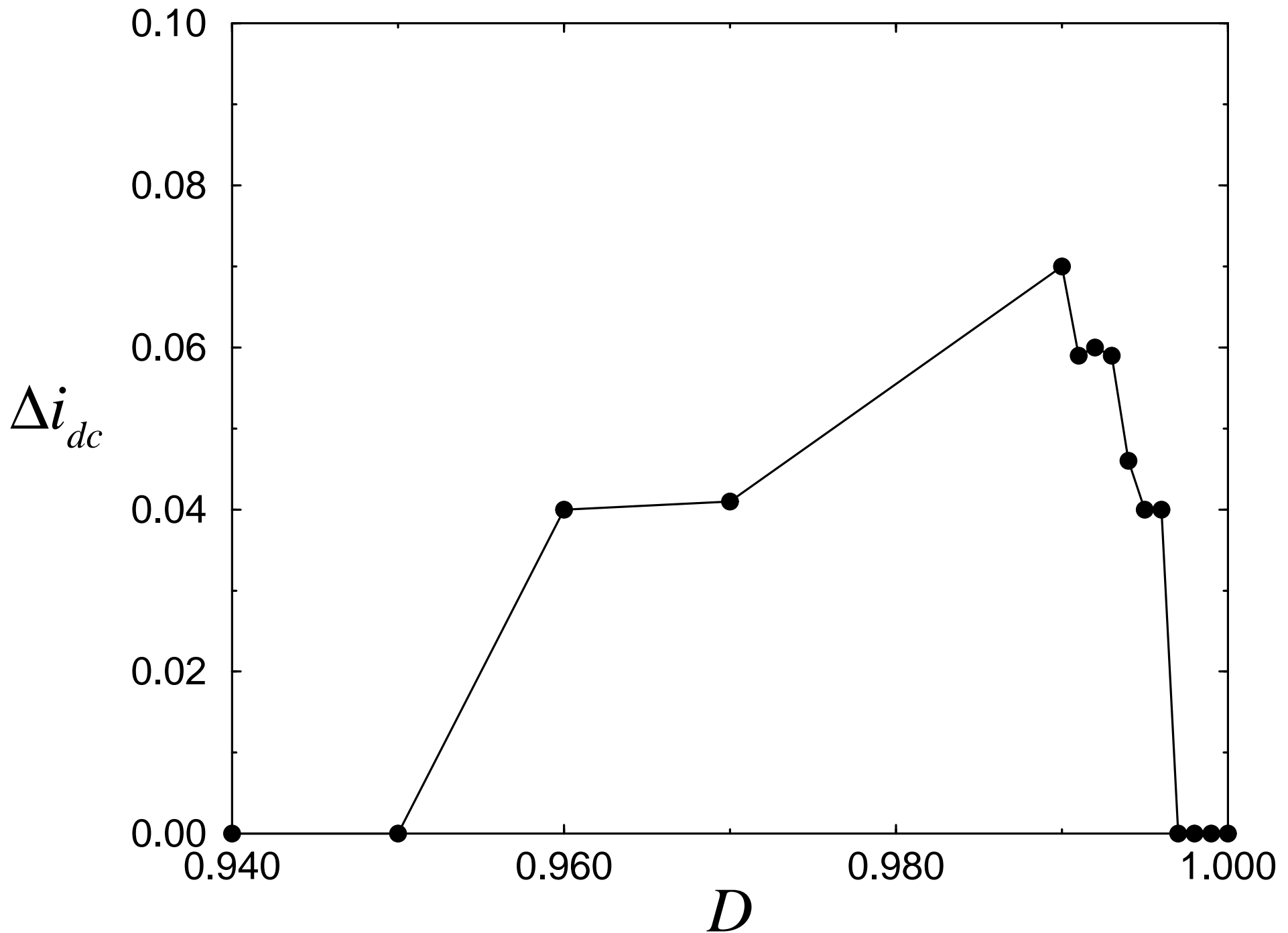


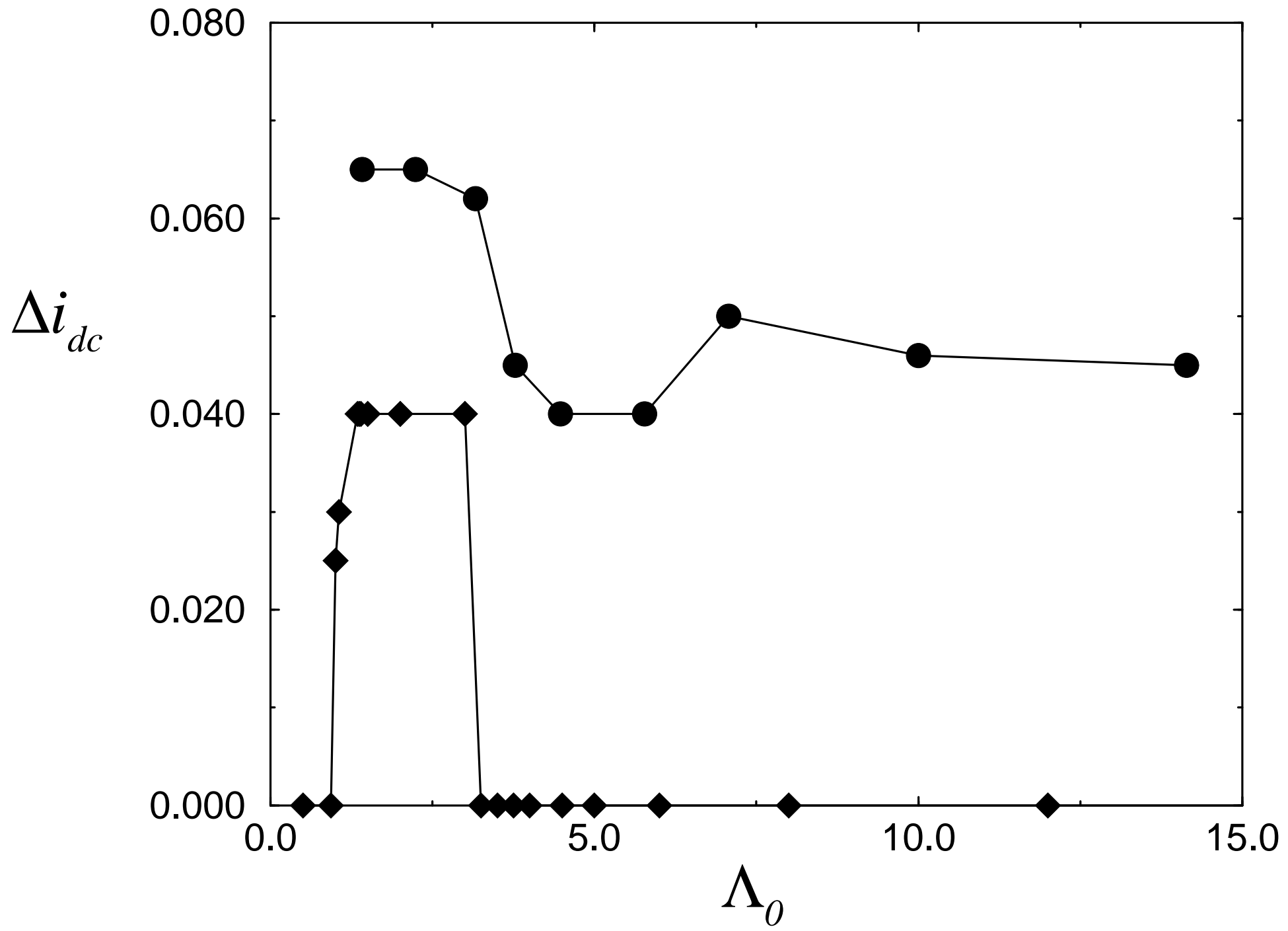


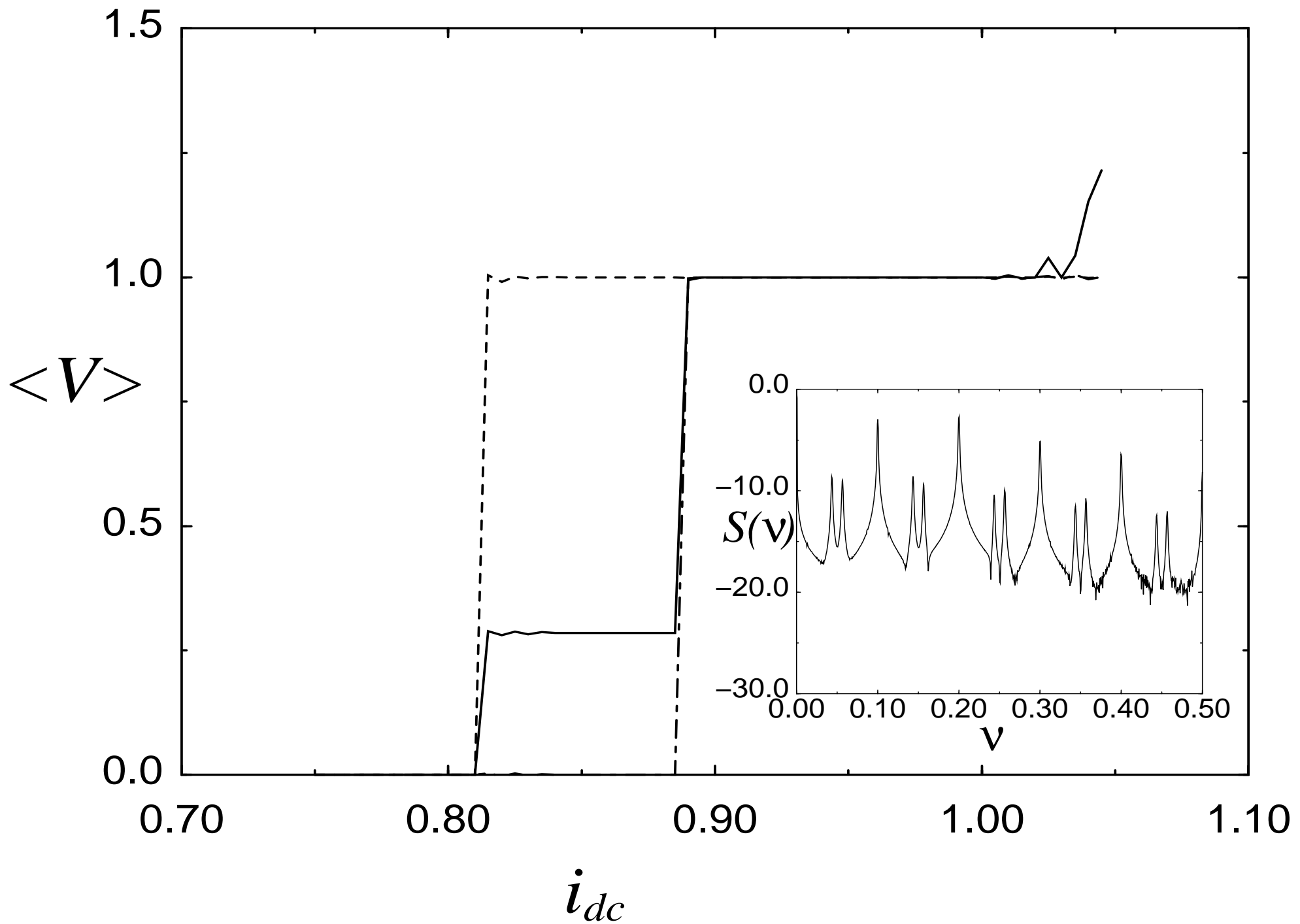


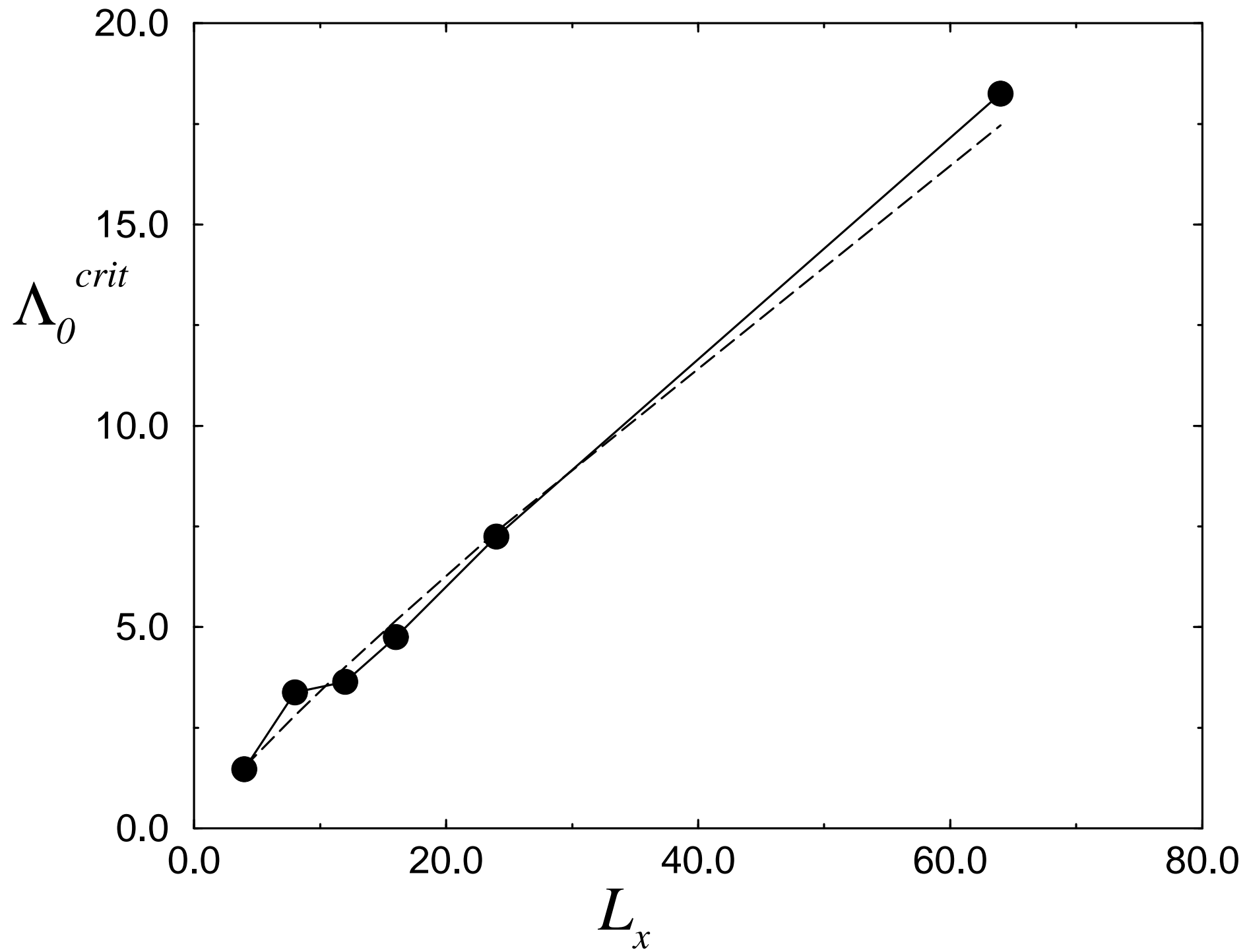


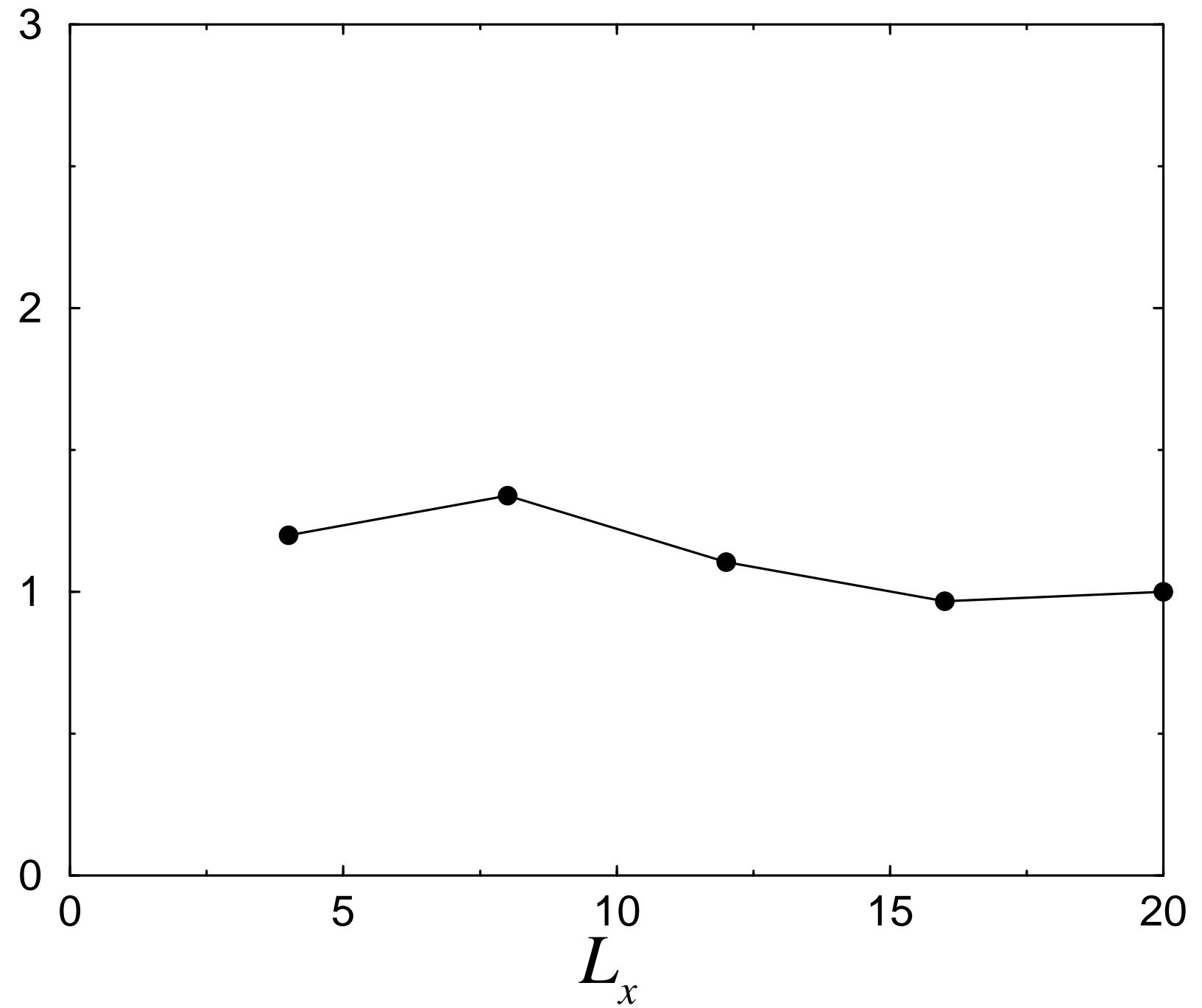


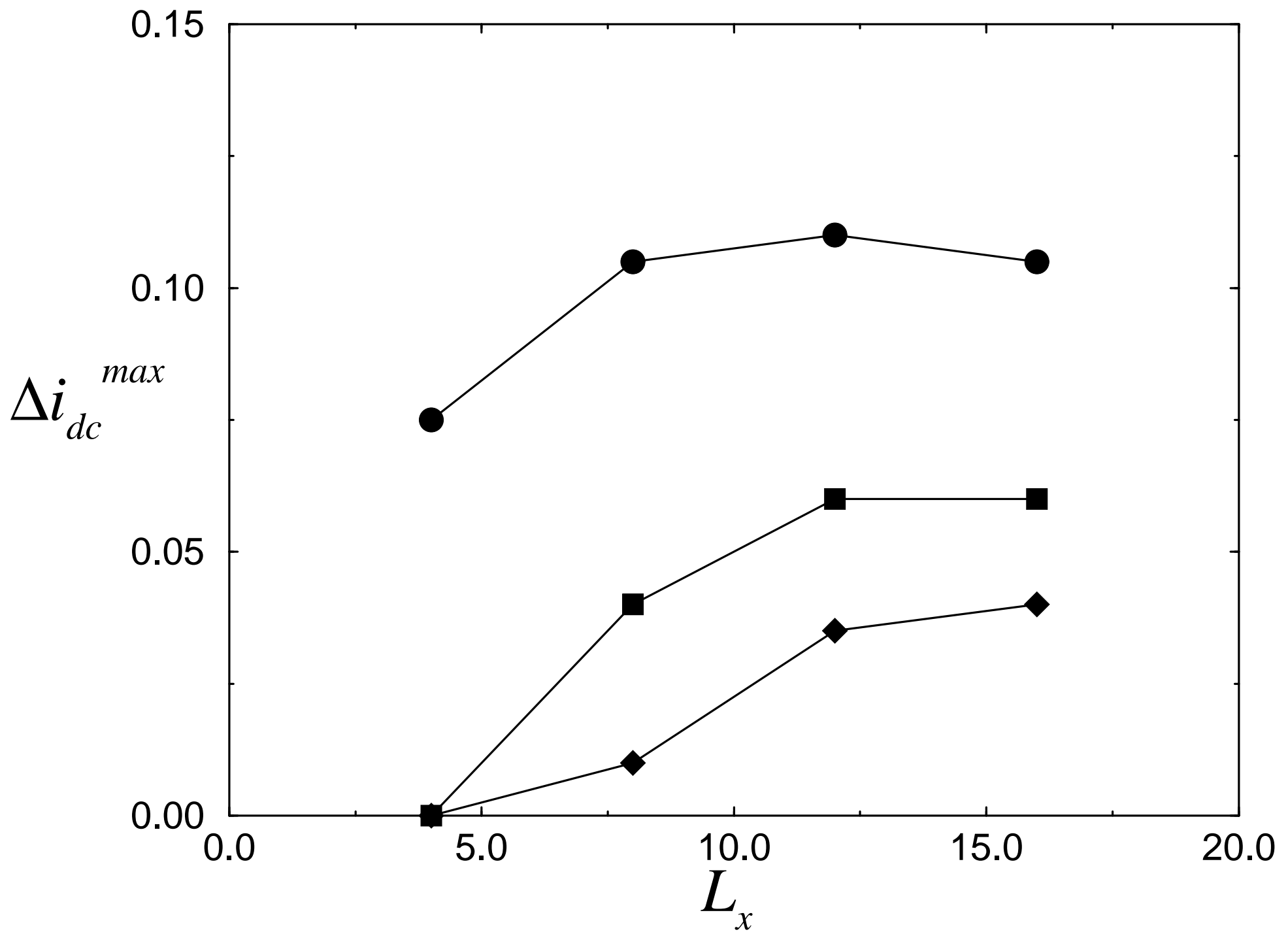








Λ_0^{max} 



Δi_{dc} 